Contributions to Mineralogy and Petrology (2021) 176:81
https://doi.org/10.1007/s00410-021-01835-z

ORIGINAL PAPER

Fluid-induced alteration of monazite, magnetite, and sulphides during the albitization of a Palaeoproterozoic granite from the Jiao-Liao-Ji orogenic belt, North China Craton

Lei Ji[1] · Fulai Liu[1] · Daniel Harlov[2,3,4] · Fang Wang[1]

Received: 12 March 2021 / Accepted: 30 August 2021 / Published online: 5 October 2021

Abstract
Monazite and magnetite are sensitive indicators of local fluid chemistry, pressure, and temperature during metasomatism. In this study, the role of fluids, during the metamorphism of a granite to metagranite, (Jiao-Liao-Ji orogenic belt, North China Craton), is explored via monazite, magnetite, and pyrite microtextures and mineral chemistry coupled with zircon and monazite Th–U–Pb dating. CL bright zircon cores (2163 ± 17 Ma) record the crystallization age of the granite. BSE dark monazite cores (1876 ± 36 Ma) are characterized by high U and Ca and low Nd contents. The surrounding BSE bright mantle (1836 ± 14 Ma) is characterized by abundant fine-grained huttonite inclusions, a high porosity, a high Th and Si content, and a low P, La, Ce, and Y content. The monazites are surrounded by a three-layered concentric corona consisting of first fluorapatite, followed by allanite, and then epidote. TiO_2 in the primary magmatic magnetite (Mag_{1-1}) has been mobilized to form a series of compositionally and texturally distinct magnetites (Mag_{1-2}, Mag_2, Mag_3, Mag_4, and Mag_5) associated with ilmenite, rutile, and titanite reaction textures. Combined, these results suggest that external NaCl and sulphate-bearing fluids derived from a local sulphate-bearing evaporate infiltrated the granite and induced the formation of pyrite and enriched the pre-existing monazite in S at around 1904 Ma. In situ $\delta^{34}S$ values for pyrite range from 13.03 ‰ to 13.41 ‰, which is typical of metamorphic pyrite. Sporadic synchysite-(Y) inclusions in the pyrite indicate a local CO_2-rich component in the fluid. The BSE bright mantle around monazite formed from later fluids from the same local evaporite deposit during the decompression stage of the Jiao-Liao-Ji orogenic belt at around ~1840 Ma, which overlaps with zircon dark rims at 1849 ± 12 Ma. This same Na-bearing fluid induced the albitization of the feldspars, formation of apatite–allanite–epidote coronas around monazite, and formation of rutile–titanite–epidote alteration textures associated with magnetite and ilmenite exsolved from the magnetite. During subsequent much later greenschist facies metamorphism, muscovite, chlorite, and Mag_5 were precipitated along mineral grain boundaries, mineral cleavage, micropores, and fractures and pyrite experienced partial alteration to goethite.

Keywords Zircon · Monazite · Apatite–allanite–epidote corona · Magnetite · Ilmenite · Titanite · Rutile · Metagranite · Jiao-Liao-Ji orogenic belt

Communicated by Daniela Rubatto.

✉ Lei Ji
jileicags@126.com

[1] Chinese Academy of Geological Sciences, Beijing 10037, China

[2] Deutsches GeoForschungsZentrum GFZ, Telegrafenberg, D-14473 Potsdam, Germany

[3] Faculty of Earth Resources, China University of Geosciences, Wuhan 430074, China

[4] Department of Geology, University of Johannesburg, Auckland Park, P.O. Box 524, Johannesburg 2006, South Africa

Introduction

Monazite [(LREE, Th, U, Ca) (P, Si)O_4] is a common accessory mineral in various types of crustal rocks, and is extremely useful for understanding and timing fluid infiltration events and subsequent mineral-fluid interaction processes (e.g., Harlov et al. 2005, 2007, 2011; Williams et al. 2007; Budzyń et al. 2010, 2011, 2017; Upadhyay and Pruseth 2012). The complex compositional zone patterns and decomposition textures preserved in monazite are generally considered to be the products of fluid-mediated element mass transfer that record the local chemistry of metasomatic/metamorphic reactions as well as date them (e.g., Broska et al. 2005; Rasmussen and Muhling 2009; Hetherington et al. 2010; Harlov et al., 2011; Williams et al., 2011; Ondrejka et al. 2012; Upadhyay and Pruseth 2012). Moreover, based on net-transfer equilibrium with garnet or xenotime and/or differences in element partitioning coefficients, monazite has been utilized to estimate metamorphic temperatures (Gratz and Heinrich 1997, 1998; Pyle et al. 2001), indicate porphyroblast (e.g., garnet and xenotime) growth or breakdown, and to investigate melt crystallization (Zhu et al. 1999; Stepanov et al. 2012; Xing et al. 2013).

Ti–Fe oxide phases (e.g., magnetite, ilmenite, and rutile) and pyrite, are pervasive in magmatic and fluid-related ore deposits. Recent studies have revealed that the crystal growth morphology of and trace element concentrations in Ti–Fe phases are sensitive to changing fluid chemistry, temperature, and pressure (e.g., Nadoll et al. 2012, 2014a,b; Hu et al. 2014, 2015b, 2017; Wen et al. 2017; Xie et al. 2017; Chen et al. 2020). However, reports of metasomatically induced partial alteration of Ti–Fe oxide minerals closely associated with the formation of apatite–allanite–epidote coronas around monazite have so far not been reported in the literature.

The aim of this study is to investigate fluid-aided processes during the metasomatic alteration and subsequent metamorphism of a granite, associated with a nearby sulphate-bearing evaporate deposit, to a metagranite in the Jiao-Liao-Ji orogenic belt, North China Craton. This is accomplished via the systematic integration of metasomatic processes involving monazite and Ti-bearing magnetite with stable S isotopic data from pyrite and geochronological data from zircon and monazite in a series of detailed petrographic observations, microtextural investigations, X-ray element mapping, electron microprobe and Raman spectral analysis.

Geological setting

The North China Craton consists of three Palaeoproterozoic tectonic belts: the khondalite belt, the trans North China orogeny, and the Jiao-Liao-Ji (JLJ) orogenic belt (Fig. 1a, Zhao et al. 2005). In the eastern North China Craton, the JLJ orogenic belt is more than 1000 km long, with a NNE-SSW strike. It divides the Eastern Block of the North China Block into the Longgang Block to the north in China and the Nangrim Block to the south in Korea (Fig. 1b; Li et al. 2005; Zhao et al. 2005, 2012).

In the JLJ orogenic belt, vigorous metamorphic fluid activity has played a key role in the formation of many large or super-large deposits, such as the Dashiqiao magnesite-talc deposit (Zhang et al. 1988; Misch et al. 2018) and the Lianshanguan uranium deposit (Cuney et al. 2012). Uranium mineralization in this deposit is closely associated with the albitization of an associated early Palaeoproterozoic granite (Zhong and Guo 1988; Cuney et al. 2012).

A series of metasedimentary and metavolcanic successions in the JLJ orogenic belt are referred to as the Liaohe Group. They are commonly considered to have been deposited between 2200 and 2000 Ma (Hu et al. 2015a; Liu et al. 2017b, 2019b; Wang et al. 2017; Xu et al. 2019). The lower portion of the Liaohe Group (Zhang 1988) contains an evaporitic sequence made up of borate, sulphides, halides, Mg-rich carbonates, and Ca–Ba sulfates (Fig. 1b; Jiang et al. 1997; Wang et al. 1998; Peng and Palmer 2002; Liu et al. 2012; Yan et al. 2014; Dong et al. 2017). The metamorphic evolution of the JLJ orogenic belt has been established from the metabasite and metapelitic rocks (Tam et al., 2011, 2012a,b,c; Cai et al., 2017; Liu et al. 2017b, 2019b; Zou et al. 2017, 2018, 2019). It displays a clockwise *P*–*T*-*t* path with prograde (2100–1960 Ma), peak (1960–1900 Ma), isothermal decompression (1900–1850 Ma), and cooling stages (1850–1800 Ma).

The metagranite described in this study is a member of the Lieryu formation, which is a part of the Liaohe Group, and is located north of the town of Taziling (N 40°51′19.75″; E 123°18′49.95″) (Fig. 1c). This location is closely associated with evaporate deposits of the Liaohe Group and is less than 30 km from the largest known uranium deposit in northeast China (Fig. 1b). The metagranite varies in width from 0.5 to ~ 1.0 m and occurs parallel to a kyanite-bearing, garnet–sillimanite micaschist and a monzonite (Fig. 2a). Due to the dissemination of goethite within mineral grain interiors, along grain boundaries, and along microfractures, the metagranite exhibits a reddish color. Thin dark veins, mainly composed of muscovite and chlorite with a thickness of ca. 1–3 mm, can be clearly observed in hand specimens (Fig. 2b).

Analytical methods

Back scattered electron (BSE) imaging

Backscattered electron (BSE) imaging of monazite breakdown textures was conducted using a ZEISS ultra plus scanning electron microscope (SEM) with an electron beam voltage of 15 kV. A 50 mm^2 OXFORD energy-dispersive spectrometer (EDS) was utilized to determine the elements present. The images were processed using INCA 4.4 (OXFORD) software. Two different brightness and contrast-level BSE images were taken in order to discern mineral zonation, mineral inclusions, and the surrounding mineral reaction textures. Discrete-color BSE images were also obtained for directly distinguishing different kinds of minerals by color.

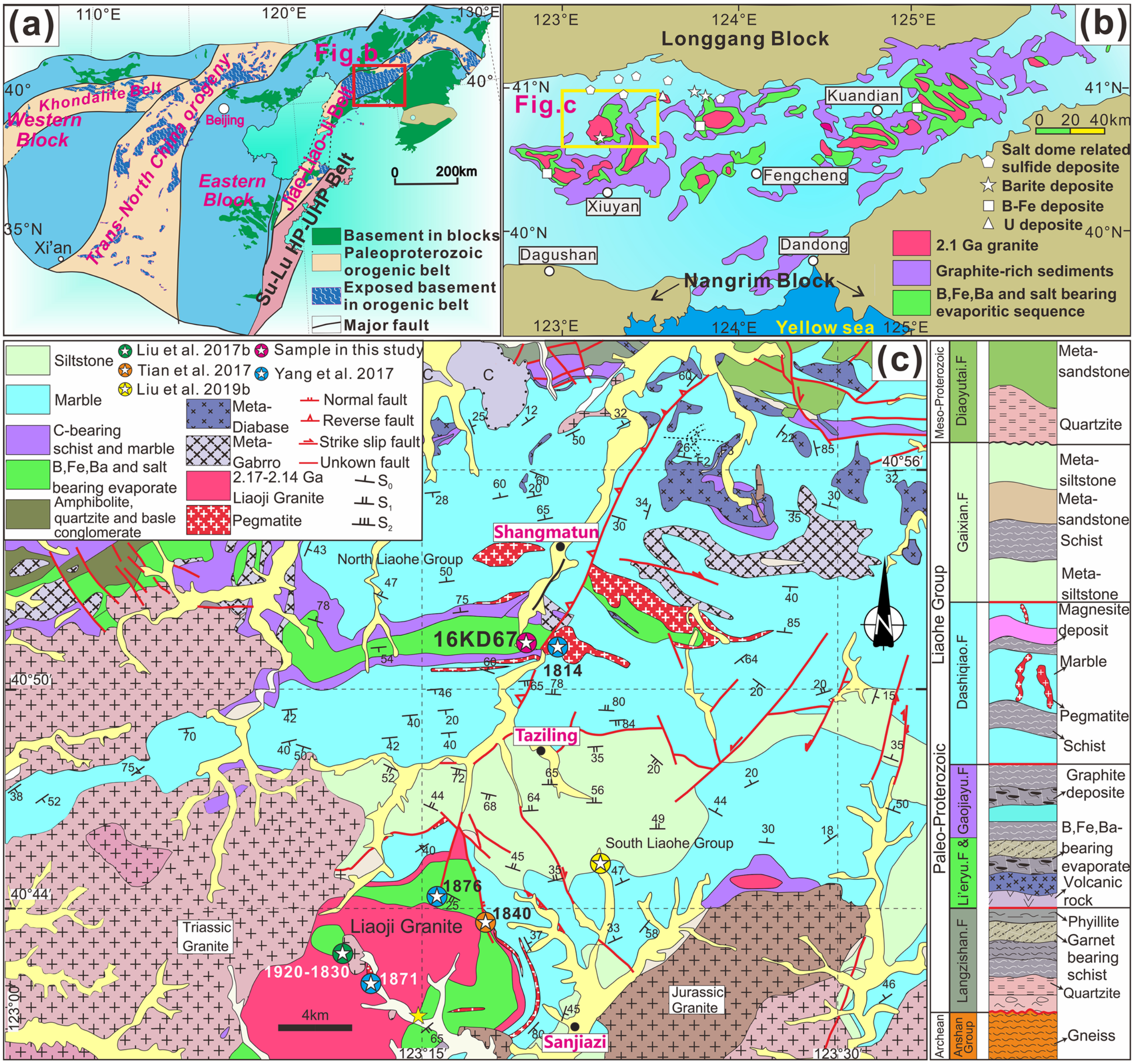

Fig. 1 **a** Tectonic subdivision of the North China Craton and adjacent regions (modified after Zhao et al. 2005, 2012). **b** The occurrence of the evaporitic sequence and graphite-rich sediments associated with the Liaohe Group (modified after Peng and Palmer 2002). The location of the salt dome and related sulfide deposits are based on Wang et al. 1998. **c** Sketched geological map of the Sanjiazi region (modified from Tian et al. 2017), eastern Liaoning Province, with the metagranite location (16KD67) marked by a star in a circle. Some granite and pegmatite ages are also marked

Electron microprobe (EMP) analysis

Representative mineral compositions from the metagranite were obtained using a JEOL JXA-8230 electron microprobe (EMP) at the Wuhan Sample Solution Analytical Technology Co., Ltd., Wuhan, China. The EMP is equipped with 6 wavelength-dispersive spectrometers. The operating conditions for REE-bearing minerals (monazite, xenotime, allanite, epidote, apatite, and huttonite), silicate minerals, ilmenite, rutile, magnetite, and pyrite were as follows: accelerating voltage of 15 kV, beam current of 50 nA, and spot size of 3 μm. The counting times for Th, U, F, Cl, Y, and REE were 30 s on the peak and 10 s at each background position. For elements in titanite, feldspar, muscovite, and chlorite, the counting times for the peak and the background positions were 10 and 5 s, respectively. Lanthanum and Ce were measured on a PETJ crystal and Pr, Nd, Sm, Eu, Gd, Tb, Dy, Ho, Er, Tm, Yb, and Lu were measured on an LIFH

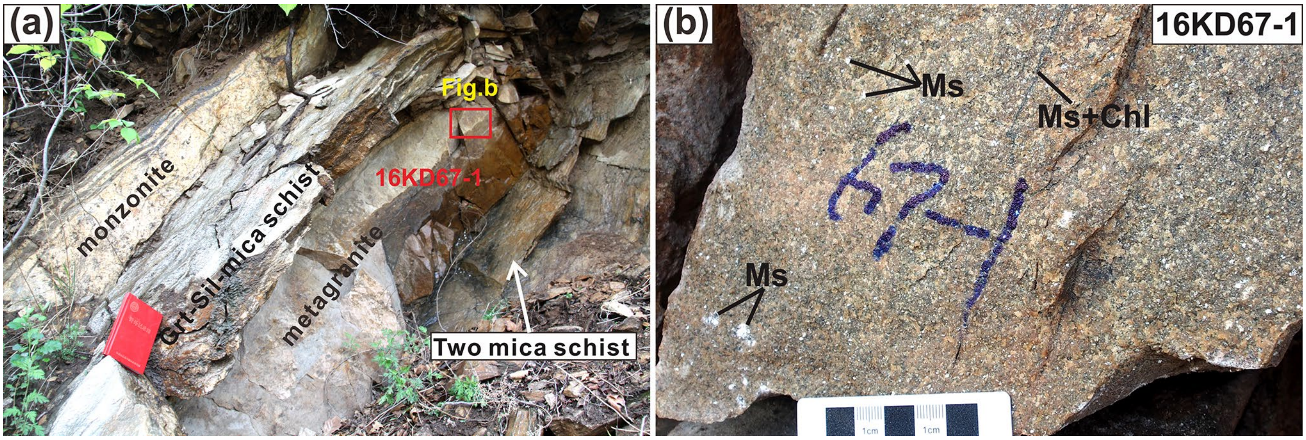

Fig. 2 Field photographs showing the occurrences of the metagranite and surrounding rocks. **a** Spatial relations between the metagranite, kyanite-bearing, garnet–sillimanite micaschist, and monzonite. **b** Muscovite and chlorite vein in the albitized metagranite. The sample position is shown in the red rectangles in Fig. 2a. Mineral abbreviations: *Chl* chlorite, *Ms* muscovite, *Grt* garnet, *Sil* sillimanite

crystal. Each element was calibrated using well-characterized natural and synthetic standards and reduced using the ZAF method.

EMP analyses of monazite, xenotime, apatite, britholite, thorite, allanite, REE-epidote, epidote, titanite, rutile, ilmenite, magnetite, goethite, pyrite, K-feldspar, plagioclase, muscovite, and chlorite along with their reaction products or inclusions are listed in Table 1 (monazite) and Supplementary Appendix S1.

X-ray compositional mapping

The internal structure of the select monazite grains and elements mapping was done using a Nova Nano SEM 450 with 50 mm^2 Max OXFORD energy-dispersive spectrometer. The operating conditions included a low-vacuum state, 15 kV acceleration voltage, and 10 nA beam current. Mapping scans used the Ca-Kα, P-Kα, Th-Mα, La-Lα, Ce-Lα, Pr-Lβ, Nd-Lα, Y-Lα, and Si-Kα X-ray intensities. Element-mapping images were processed using the software AZtecLive version 3.0.

Raman spectral analysis

Fine-grained mineral inclusions in pyrite and magnetite were identified by Laser Raman at the Mirco-Raman Lab in the Institute of Geology, Chinese Academy of Geological Sciences, Beijing, China using an Horiba spectrometer LabRAM HR evolution equipped with an Olympus BX41 light microscope. Raman spectra were excited using a 532.02 nm Nd: YAG laser with a beam diameter of 1 µm, 100 mW laser power, and acquired via a 600 gr/mm optical grating through an 80 m confocal hole. The data were processed using LabSpec 6 software.

In situ S isotope analysis

In situ S isotopic analyses of pyrites were performed using a Neptune Plus MC–ICP–MS (Thermo Fisher Scientific, Bremen, Germany) equipped with a Geolas HD excimer ArF laser ablation system (Coherent, Göttingen, Germany) and nine Faraday cups at the Wuhan Sample Solution Analytical Technology Co. Ltd, Wuhan, China. Helium was used as the carrier gas for the ablation cell and was mixed with Ar after the ablation cell. Single spot ablation mode was used. Large spot size (44 µm) and slow-pulse frequency (2 Hz) were used to avoid the down-hole fractionation effect (Fu et al. 2016). 100 laser pulses were completed in one analysis. A new signal-smoothing device was used downstream from the sample cell to efficiently eliminate short-term variations in the signal, especially for slow-pulse frequency conditions (Hu et al. 2015c). The laser fluence was kept constant at ~5 J/cm^2. Pyrite standard PPP-1 (Fu et al. 2016) was used as the reference material for correcting the acquired data. In addition, the in-house reference material SP-Py-01 ($\delta^{34}S_{V\text{-}CDT} = 2.0‰ \pm 0.4‰$), was analyzed repeatedly as an unknown sample to verify the accuracy of the calibration. Sulfur isotope ratios are reported as $\delta^{34}S$ relative to the Vienna Canyon Diablo Troilite (V-CDT) and are listed in Supplementary Appendix S2.

Table 1 Representative monazite and xenotime EMP Analyses (wt%)

Zone	Mnz_D						Mnz_C				Mnz_B						Mnz_G				Mnz_L	
#Pts	5	3	4	2	2	1	2	3	4	2	4	4	4	3	4	2	4	1	4	2	1	1
P_2O_5	29.04	29.04	28.82	28.61	26.53	28.56	27.67	27.46	27.26	27.02	24.99	24.69	24.51	24.67	26.43	28.41	27.64	26.55	27.91	28.08	29.20	28.33
SiO_2	0.02	0.02	0.01	0.02	1.55	0.22	0.97	1.02	1.19	1.25	2.53	2.62	2.44	2.80	1.73	0.62	0.91	1.70	0.86	0.69	0.02	0.11
ThO_2	4.43	3.39	4.11	3.89	10.97	4.07	8.30	8.75	9.32	9.46	14.61	14.80	14.67	15.72	10.16	5.72	9.92	11.74	9.08	8.86	7.46	5.88
UO_2	1.08	1.06	1.10	1.08	0.60	0.29	0.43	0.47	0.54	0.50	0.69	0.71	0.84	0.78	0.13	0.04	0.64	0.59	0.56	0.65	2.54	2.67
SO_3	0.23	0.27	0.28	0.24	0.00	0.54	0.00	0.00	0.00	0.00	0.00	0.00	0.00	0.00	0.00	0.00	0.00	0.00	0.00	0.00	0.11	0.09
Y_2O_3	1.69	1.70	1.75	1.57	1.54	2.20	2.07	2.00	1.91	1.80	1.28	1.17	1.22	1.23	1.04	0.30	2.23	1.62	1.80	2.29	1.28	0.74
La_2O_3	14.32	14.34	14.40	14.35	12.00	13.41	12.72	12.39	12.50	12.36	11.27	11.30	11.43	10.89	12.86	13.73	11.89	11.45	12.60	12.12	13.79	15.31
Ce_2O_3	28.95	29.48	29.06	28.96	26.23	28.97	27.24	26.82	26.88	26.50	24.92	24.93	25.31	24.21	27.88	30.02	25.70	25.58	26.56	25.86	25.99	27.39
Pr_2O_3	3.16	3.26	3.24	3.24	2.82	3.03	3.01	3.01	2.97	2.96	2.78	2.78	2.78	2.72	3.06	3.35	2.84	2.86	2.97	2.92	2.92	3.09
Nd_2O_3	10.62	10.93	10.43	10.83	10.78	11.23	11.12	10.94	10.79	11.04	10.66	10.60	10.63	10.40	11.76	12.69	10.57	11.11	10.64	10.46	9.12	9.29
Sm_2O_3	1.59	1.63	1.59	1.59	1.61	1.66	1.70	1.71	1.67	1.63	1.57	1.47	1.50	1.53	1.69	1.84	1.72	1.64	1.60	1.67	1.40	1.37
Eu_2O_3	0.11	0.14	0.10	0.10	0.00	0.02	0.00	0.00	0.00	0.00	0.00	0.00	0.01	0.00	0.00	0.00	0.02	0.00	0.02	0.04	0.09	0.00
Gd_2O_3	2.21	2.26	2.23	2.24	2.10	2.23	2.16	2.17	2.12	2.15	1.94	1.93	1.95	1.88	2.18	2.33	2.14	2.09	2.13	2.11	2.05	2.03
Tb_2O_3	0.17	0.15	0.15	0.14	0.17	0.23	0.19	0.17	0.21	0.19	0.17	0.11	0.14	0.17	0.15	0.10	0.19	0.13	0.18	0.23	0.13	0.16
Dy_2O_3	0.45	0.42	0.43	0.47	0.45	0.83	0.55	0.55	0.52	0.53	0.31	0.34	0.37	0.34	0.43	0.17	0.60	0.32	0.49	0.66	0.30	0.28
Er_2O_3	0.13	0.14	0.14	0.14	0.14	0.25	0.08	0.14	0.13	0.14	0.12	0.09	0.09	0.09	0.08	0.02	0.17	0.12	0.15	0.17	0.07	0.04
CaO	1.48	1.27	1.41	1.37	1.18	1.32	1.16	1.13	1.11	1.08	1.11	1.06	1.02	1.09	0.74	0.78	1.63	1.29	1.43	1.61	2.44	2.18
SrO	0.01	0.03	0.01	0.01	0.01	0.00	0.00	0.00	0.00	0.00	0.00	0.00	0.01	0.00	0.00	0.04	0.01	0.00	0.02	0.01	0.03	0.06
FeO	0.03	0.06	0.00	0.04	0.06	0.08	0.03	0.08	0.02	0.01	0.05	0.08	0.02	0.05	0.13	0.06	0.09	0.08	0.00	0.08	0.06	0.02
PbO	0.67	0.60	0.66	0.63	1.11	0.45	0.84	0.92	0.94	0.95	1.44	1.37	1.23	1.54	0.38	0.29	1.05	1.09	0.97	0.95	1.37	1.30
Sum	100.4	100.2	99.9	99.5	99.8	99.6	100.3	99.7	100.1	99.6	100.4	100.0	100.2	100.1	100.8	100.5	100.0	99.9	99.9	99.5	100.4	100.3
X_{Chrl}	14.27	12.30	13.73	13.26	11.55	12.94	11.38	11.12	10.87	10.64	10.84	10.39	9.92	10.73	7.15	7.47	15.90	12.58		15.87	23.23	20.54
X_{hut}	0.00	0.00	0.00	0.00	7.60	0.00	4.41	5.24	6.00	6.27	12.17	12.58	12.55	13.75	7.48	2.47	4.26	7.83		3.17	0.10	0.00
X_{Mnz}	85.73	87.70	86.27	86.74	80.85	87.06	84.21	83.64	83.13	83.09	76.99	77.03	77.53	75.52	85.37	90.07	79.84	79.59		80.96	76.67	79.46
T (℃)	680	660	703	633	674						584	519	543	572								

1σ standard deviation in italics, a = total Fe as FeO, blank = below EMP detection limit. Temperature calculated by Y in monazite geothermometer (Gratz and Heinrich 1997) Mnz_D, Mnz_C, Mnz_B, Mnz_G and Mnz_L represent monazite dark core, concentric zone, bright mantle, gray rim and light areas in dark core under BSE image. Xchrl = 100 × (2Ca)/D; XHut=100 × (Th+U+Pb−Ca)/D, D= [REE+2Ca+(Th+U+Pb−Ca)

U–Pb laser ablation inductively coupled plasma-mass spectrometer (LA-ICPMS) dating of monazite and zircon

U–Pb dating of monazite from the metagranite was using a GeolasPro laser ablation system that consists of a COMPexPro 102 ArF excimer laser (wavelength of 193 nm) and a MicroLas optical system. An Agilent 7700e ICP-MS instrument was used to acquire ion-signal intensities. Helium was applied as a carrier gas. Argon was used as the make-up gas and mixed with the carrier gas via a T-connector before entering the ICP. A "wire" signal smoothing device is included in this laser ablation system. The spot size and frequency of the laser were set to 16 µm and 2 Hz, respectively. Monazite standard 44,096 and glass NIST610 were used as external standards for U–Pb dating and trace element calibration, respectively. Each analysis incorporated a background acquisition of approximately 20–30 s followed by 50 s of data acquisition from the sample. An Excel-based software ICPMSDataCal was used to perform off-line selection and integration of background and analyzed signals, time-drift correction and quantitative calibration for trace element analysis and U–Pb dating (Liu et al. 2010). Monazite U–Pb ages of the monzonite and kyanite-bearing, garnet–sillimanite micaschist were measured using an ELEMENT-XR inductively coupled plasma-mass spectrometer (ICP-MS) attached to a 200 nm femtosecond laser ablation (LA) system at the Department of Solid Earth Geochemistry, Japan Agency for Marine-Earth Science and Technology, Yokosuka, Japan. A secondary multiplier with counting mode was utilized for measuring ^{202}Hg, ^{204}(Pb + Hg), ^{206}Pb, ^{207}Pb, ^{208}Pb, ^{232}Th, and ^{238}U. A 10 µm laser beam with 6 J/cm^2 was rotated along the circumference of a circle with a 5 µm radius at a velocity of 2.1 µm at 1 and 3 Hz, resulting in a 20 µm ablation pit. To reduce elemental fractionation due to defocusing during the laser ablation process, a rotation raster ablation protocol was applied (Kimura et al. 2011). In this protocol, each analysis consisted of 30 s gas blank measurements followed by ca. 90 s laser ablation sampling. In total, three analyses of monazite 44,069 (Aleinikoff et al. 2006), one analysis of the Manangotry monazite (Horstwood et al. 2003), and one analysis of the 16-F-6 monazite (Simonetti et al. 2006) were inserted at intervals of every 10 analyses for the monazite. The specific correction technique for common Pb and analytical uncertainties has been described by Itano et al. (2016).

LA-ICPMS U–Pb dating of zircons was conducted using an AnlytikJena PQMS Elite ICPMS instrument with an ESI NWR 193 nm LA system at Beijing Createch Testing Technology Co. Ltd., Beijing, China. The laser beam diameter was 25 µm and was operated at a frequency of 10 Hz. Helium was applied as a carrier gas. Argon was used as the make-up gas and mixed with the carrier gas via a T-connector before entering the ICP. Each analysis consisted of about 15 s of background acquisition and 45 s of data acquisition. Each set of 5–10 analyses was followed by analyses of the glass standard NIST610 and the zircon standards GJ-1, 91,500, and Plešovice (Hu et al. 2008). The U–Pb concordia plots were processed with Isoplot 3.0, and the data are presented in Supplementary Appendix S3 with 1σ errors and 95% confidence limits (Ludwig 2003).

Silicate petrology and petrography of the metagranite

On the thin-section scale, the most striking feature in the metagranite is the extensive albitization of the plagioclase (Fig. 3a, b) and the heterogeneous distribution of minerals (see Fig. S1 in Supplementary Appendix S4). Albitization dominantly occurs in the cores of the plagioclase. The boundaries between the Na-rich core and Ca-richer rims are distinct and sharp (Fig. 3a, b). In the Ab–Or–An diagram (see Fig. S2 in Supplementary Appendix S4), the albitized plagioclase cores plot between An_1 and An_{10}, with an average of An_4. The BSE brighter rims have distinctly higher An values (An = 18–19) corresponding to oligoclase (Supplementary Appendix S1). Occasionally, anti-perthite is seen in the core of the plagioclase grains. Feldspar in the immediate vicinity of muscovite–chlorite veins is near end member K-feldspar. Relative to plagioclase, K-feldspar is minor, and only a few fine grains are found near the muscovite–chlorite vein or occur peripherally to the plagioclase grains (see Fig. S1b in Supplementary Appendix S4).

Thin sections from the metagranite can be subdivided into a coarse muscovite-rich region, a quartz- and chlorite-rich domain, and a quartz-rich chlorite-absent domain. Muscovite in the metagranite shows a broad grain size range from 0.1 mm to 5 mm. In the quartz-rich region, varying degrees of chloritization accompany the magnetite and epidote along the muscovite cleavages (Fig. 3c, d). In the thinner veins, muscovite fills the centre, and chlorite occurs along the flanks. The muscovite–chlorite veins also cut through pre-existing coarse-grained muscovite. Allanite occurs along cleavages in the muscovite. Locally, fine-grained monazite and allanite can be found sporadically distributed in the chlorite zone (see Fig. S1b in Supplementary Appendix S4).

Coarse muscovite is characterized by the lowest SiO_2, FeO, and MgO and the highest Al_2O_3 and TiO_2 contents, which range between 45.17 and 47.46 wt%, 4.09–4.86 wt%, 0.59–0.90 wt%, 30.34–33.40 wt%, and 0.82–1.33 wt%, respectively (Supplementary Appendix S1). Compared with the coarse muscovite, fine-grained muscovite, accompanied by albite, shows a slight increase in FeO but still has a lower FeO content than muscovite near magnetite and pyrite. The

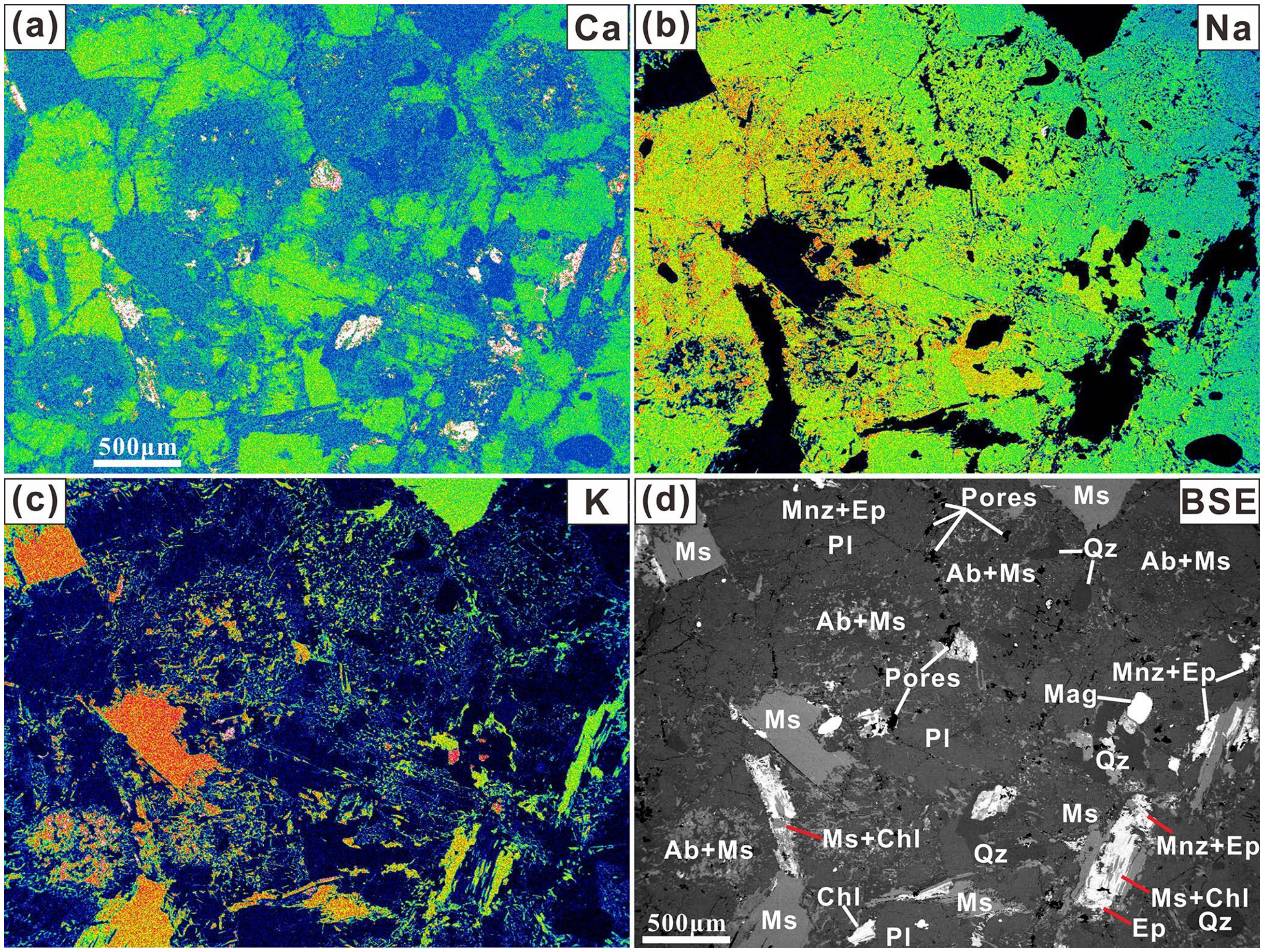

Fig. 3 X-ray element maps for **a** Ca, **b** Na, **c** K, and corresponding **d** BSE image of albitization and chloritization in the metagranite. Mineral abbreviations: *Ab* albite, *Ep* epidote, *Mnz* monazite, *Pl* plagioclase, *Qz* quartz

muscovite vein exhibits a narrow SiO_2 and Al_2O_3 compositional range and has the highest FeO content (6.95–9.51 wt%). Retrograde, fine-grained muscovite shows a slightly lower Ti content than that of fresh coarse-grained muscovite. However, the skeletal muscovite associated with magnetite has a higher Ti and Fe content compared to the coarse muscovite. Chlorite in muscovite cleavages has Al contents between 17.66 and 19.52 wt%, such that Al on the tetrahedral position ranges from 1.00 to 1.16 (apfu).

Quartz grains commonly exhibit irregular, lobate grain boundaries or occur as inclusions in muscovite or albitized plagioclase. Pervasive fractures and vugs or interstices quartz may remain after the dissolution of some minerals.

Phosphate, oxide, and sulphide mineralogy of the metagranite

Monazite, xenotime, and huttonite

In the metagranite, monazite occurs as euhedral to subhedral inclusions within the feldspar and muscovite. The monazite crystals are 30–200 µm long with length to width ratios of ~1:1–4:1. Inclusions in the monazite dominantly consist of fluorapatite and huttonite ($ThSiO_4$) (Fig. 4) where the huttonite is a metastable phase. Inclusions of xenotime can also occur in the monazite (Fig. S3 in Supplementary Appendix S4). More than 300 monazite grains were documented under BSE imaging in two thin sections. Most of the grains display a distinct BSE dark core with a lighter area, which in turn is surrounded by a BSE gray concentric oscillatory zone, and then surrounded by a BSE bright mantle with a BSE darker gray rim (Fig. 4a, b, c). Altered domains in the monazite can

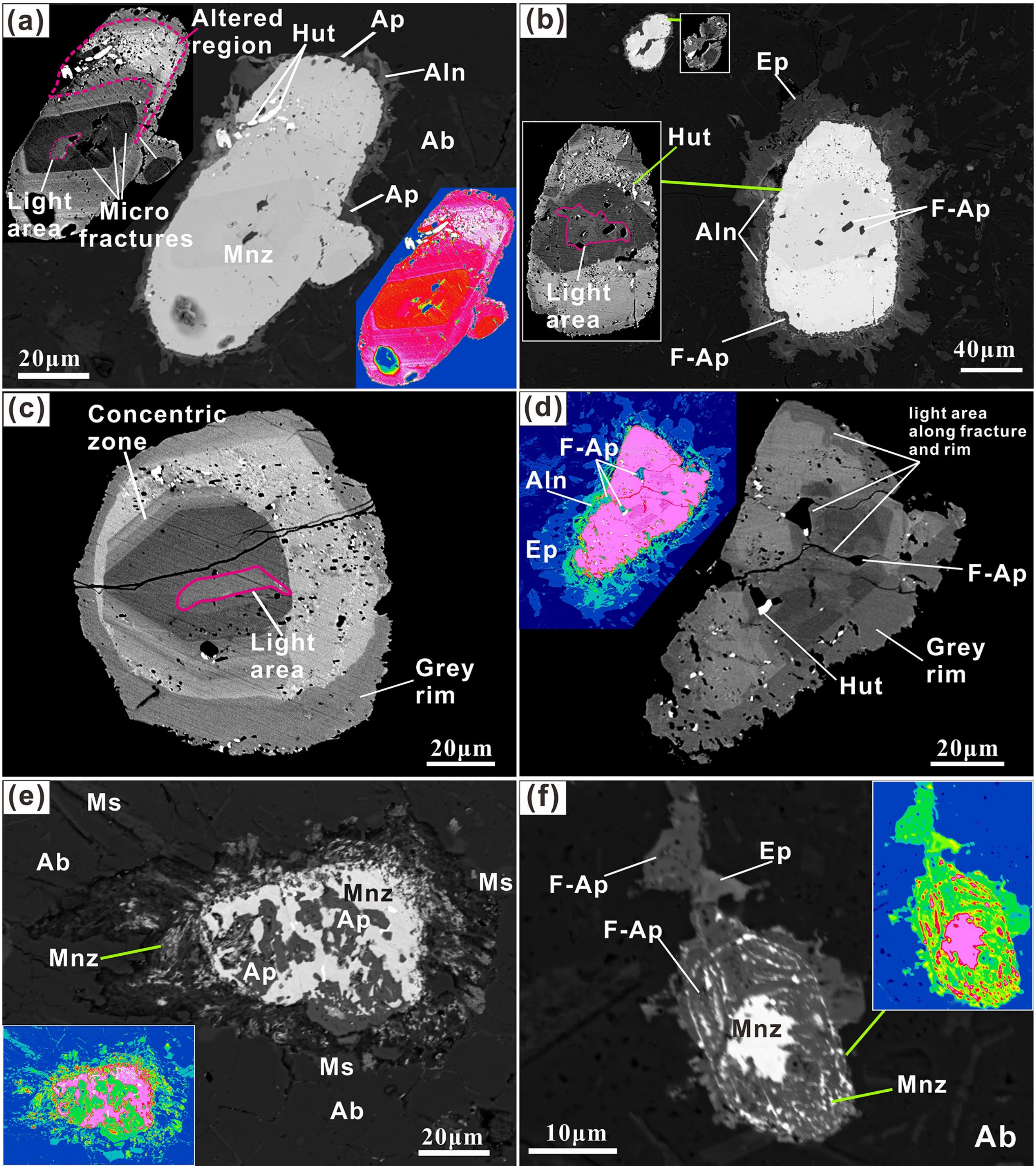

Fig. 4 BSE images showing various examples of altered monazite from the metagranite. **a** Monazite showing regions of alteration rich in porosity along with huttonite inclusions. **b** Monazite with fine-grained inclusions and extensive porosity in the altered area, which is rimmed by an apatite, allanite, and epidote corona. **c** Monazite with BSE bright, BSE gray, BSE dark, and BSE light regions. A high porosity and fine-grained huttonite inclusions are characteristic of the altered areas. **d** Monazite with a BSE dark core and BSE bright mantle showing alteration along fractures and numerous huttonite inclusions. A BSE gray rim truncates earlier domains. **e** Primary monazite partially replaced by secondary apatite with a corona of REE epidote and muscovite. **f** Monazite partially replaced by secondary apatite with small remnants of secondary monazite. Mineral abbreviations: *F-Ap* fluorapatite, *Aln* allanite; *Hut* huttonite

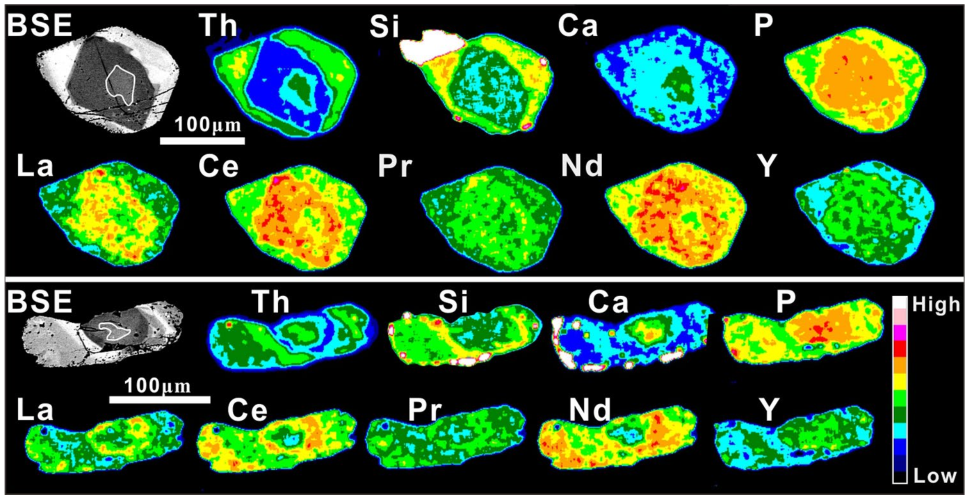

Fig. 5 BSE images and Th, Si, Ca, P, La, Ce, Pr, Nd, and Y mapping of two monazites from the metagranite. Warmer colors indicate higher element concentrations

be easily distinguished from other regions by extensive, BSE bright, fine-grained inclusions, and a high porosity.

A three-layered corona structure consisting of successive concentric zones of first apatite, followed by allanite, REE-epidote, and then epidote surrounds a subset of the monazite grains. The apatite layer consists of a narrow band (< 20 µm) that follows the original shape of the monazite grain. Apatite can also partially/totally replace the monazite leaving behind fine-grained (< 0.5 µm) remnants of monazite in an apatite matrix (Fig. 4e, f). The apatite zone is surrounded by a few- to tens-of-microns-wide allanite ring, which grades into REE epidote and then epidote (Fig. 4a, d). Locally, allanite rimmed by epidote can also be observed along muscovite cleavage planes (see Fig. S1b in Supplementary Appendix S4). The width of the epidote zone can vary from a few microns to several hundreds of microns. Formation of these apatite–allanite–epidote coronas surrounding the monazite took place via the following generalized reaction:

$$\begin{aligned} &\text{Monazite} + \text{Muscovite} + \text{Anorthite(in Plagioclase)} \\ &\quad + F\text{(in fluid)} \rightarrow \text{Fluorapatite} + \text{Allanite} \qquad (1) \\ &\quad + \text{Epidote} + \text{Th - silicate} + \text{Quartz}. \end{aligned}$$

Five distinct domains (the BSE dark core, along with BSE light areas, followed by a BSE gray concentric oscillatory zone, BSE bright mantle, and BSE gray rim) of seven zoned monazite grains from the metagranite were systematically analyzed by EMP. The variation trends from core to rim of four representative grains are illustrated in Fig. S4 (Table 1, see also Supplementary Appendix S1 and S4). Among the five regions, the BSE dark core was characterized by the highest LREE and P_2O_5 (28.29–29.54 wt%) and lowest ThO_2 (2.78–4.94 wt%), SiO_2 (0–0.03 wt %), and PbO (0.53–0.74 wt%) concentrations. It was also the only domain in which the S content exceeded the detection limit (Table 1). In contrast, BSE light areas in the BSE dark core show significant differences in higher UO_2 (2.54–2.67 wt%) and CaO (2.18–2.44 wt%), and lower Nd_2O_3 (9.12–9.29 wt%) and Sm_2O_3 (1.37–1.40 wt%) compared to the other zones (Fig. 5). The concentric BSE gray oscillatory zone surrounding the BSE dark core has the lowest UO_2 content (0.43–0.60 wt%) in all domains. The altered BSE bright mantle surrounding the BSE gray oscillatory zone has high ThO_2 (13.06–16.67 wt%) and SiO_2 (2.17–2.93 wt%) contents with correspondingly lower P_2O_5 (23.61–25.70 wt%), LREE, and CaO (0.92–1.16 wt%) values. In contrast, the BSE gray rim shows element values intermediate between those of the core and the mantle (Table 1). The Gd fraction ($X_{Gd} = Gd/\sum REE$) exhibits an extremely narrow range (0.037–0.041) no matter which zone it is measured in (Supplementary Appendix S1).

On the REE + P + Y vs. Th + U + Si diagram (Fig. 6a), the concentric zone, BSE gray rim, and BSE bright mantle indicate that the huttonite substitution dominates. The ThO_2 content exhibits the broadest variation (2.78–16.67 wt %) between the BSE dark core, BSE bright mantle, and BSE gray rim. It has a positive correlation with SiO_2 (Fig. 6b).

The xenotime inclusions in the monazite have Y_2O_3 contents ranging from 34.47 to 44.70 wt% and molar proportions of Y^{3+} between 34.0 and 40.6 (Supplementary Appendix S1). The positive correlation between (U + Th) and Si (Fig. 6b) indicates the presence of the thorite ($ThSiO_4$) and coffinite ($USiO_4$) components in xenotime. Thorite inclusions have ThO_2 contents ranging from 64.15 to 73.32 wt% and SiO_2 contents ranging from 10.45 to 16.86 wt%. The REE contents in thorite ranges 1.75–11.21 wt% and exhibit inverse correlation with ThO_2 contents (Supplementary Appendix S1). Utilizing the Y in monazite geothermomenter of Gratz and Heinrich (1997) for monazite co-existing with the xenotime inclusions gives a range of estimated temperatures ranging from 633 to 703 °C and 519 to 584 °C

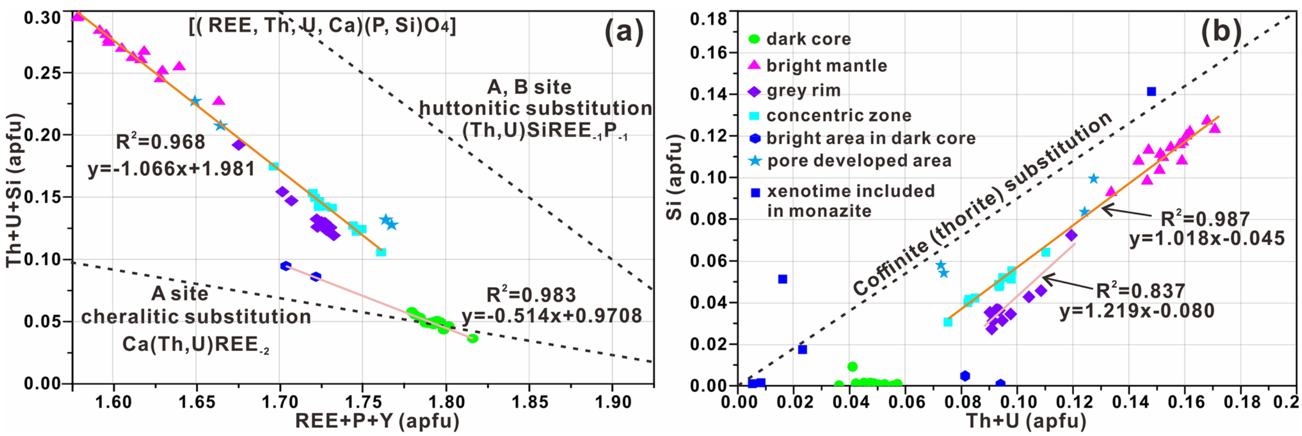

Fig. 6 Compositional plot of monazite and xenotime from the albitized granite. **a** Th + U + Si vs. REE + Y + P plot (atomic proportions) showing the ideal cheralite and thorite/huttonite substitution vectors (straight lines). **b** Th + U vs. Si substitution diagram for monazite and xenotime. The thorite substitution is given by the dashed line

for the BSE dark core and BSE bright mantle, respectively (Table 1).

Apatite, allanite, and epidote

Apatite in the coronas surrounding the monazite have LREE (La-Sm) + Y_2O_3 contents ranging from 0.32 to 6.44 wt% that exhibit a negative correlation with the P_2O_5 and CaO. The F content in apatite ranges from 0.98 to 3.95 wt%, corresponding to 0.41 to 1.66 atoms per formula unit (apfu) (Supplementary Appendix S1). The Cl content is mostly below the EMP detection limit. Based on charge balance calculated on the halogen site, the OH content are ranges from 0.27 to 0.59. Apatite is also found as inclusions in the monazite and well as intergrown with monazite (Fig. 4b, d). However it was too small for accurate EMP analysis, without being affected by the surrounding monazite.

Allanite and epidote cations and type were calculated using the WinEpclas program (Yavuz and Yildirim 2018). The mean composition of each epidote type, and the corresponding cation ratios, are listed in Supplementary Appendix S1 and illustrated in Fig. S5 (Supplementary Appendix S4). Based on the REE + Y_2O_3 content, the epidote can be subdivided into allanite, REE-bearing epidote, epidote, and clinozoisite. According to Ce–Y–Nd classification, the allanite-(Ce) exhibits Ce contents between 6.49 and 11.93 wt%, SiO_2 contents between 31.31 and 35.69 wt%, Al_2O_3 contents between 14.39 and 21.01 wt%, and REE + Y_2O_3 contents between 14.65 and 25.29 wt% (Supplementary Appendix S1). Allanite in the corona grades into REE-epidote (REE + Y_2O_3 = 5.91 – 12.55 wt%).

Magnetite, ilmenite, rutile, and titanite

In the metagranite, the monazite breakdown textures are often intimately associated with magnetite alteration microstructures. These magnetite alteration microstructures are concentrated in the chlorite- and quartz-rich domains (Fig. S1a). Six types of magnetite can be identified in the metagranite (Supplementary Appendix S1). These include (1) primary euhedral, magmatic magnetite (Mag_{1-1}), which contains ilmenite exsolution lamellae as well as ilmenite along the grain rim (Fig. 7a); (2) Mag_{1-2}, which has a partly preserved exsolution texture with abundant, elongated, parallel-aligned ilmenite and rutile lamellae (Fig. 7b, c) (3) Mag_2, which ranges in size from 200 to 800 µm and commonly exhibits intergrowth with lamellae consisting of rutile–ilmenite symplectite along the {111} plane (Fig. 7d), (4) Subhedral inclusion-free magnetite (Mag_3), which is found in titanite associated with retrograde Mag_{1-2}, (5) Ragged magnetite (Mag_4), which features etch pits and fine-grained inclusions of barite, galena, and sphalerite (Fig. 7e); and lastly (6) euhedral magnetite (Mag_5) grains, which range in size from 50 to 200 µm, and are associated with chloritized muscovite (Fig. 7f). A three-layered corona texture surrounds Mag_{1-2} consisting first of rutile, followed by ilmenite + rutile, then titanite, and finally, epidote. Surrounding this reaction texture, flaky muscovite and chlorite are also observed (Fig. 7c).

Chemically, the different magnetite types can be distinguished from each other by their TiO_2, V_2O_3, and Cr_2O_3 content (Fig. S6a; Supplementary Appendix S1). Magmatic Mag_{1-1} is characterized by high TiO_2 contents ranging from 6.90 to 7.31 wt %, while the partly metasomatically altered Mag_{1-2} has TiO_2 contents ranging from 1.03 to 5.43 wt % (average 1.99 wt %). Both Mag_{1-1} and Mag_{1-2} exhibit high V_2O_3 values, which range from 0.15 to 0.17 and 0.10 to 0.16

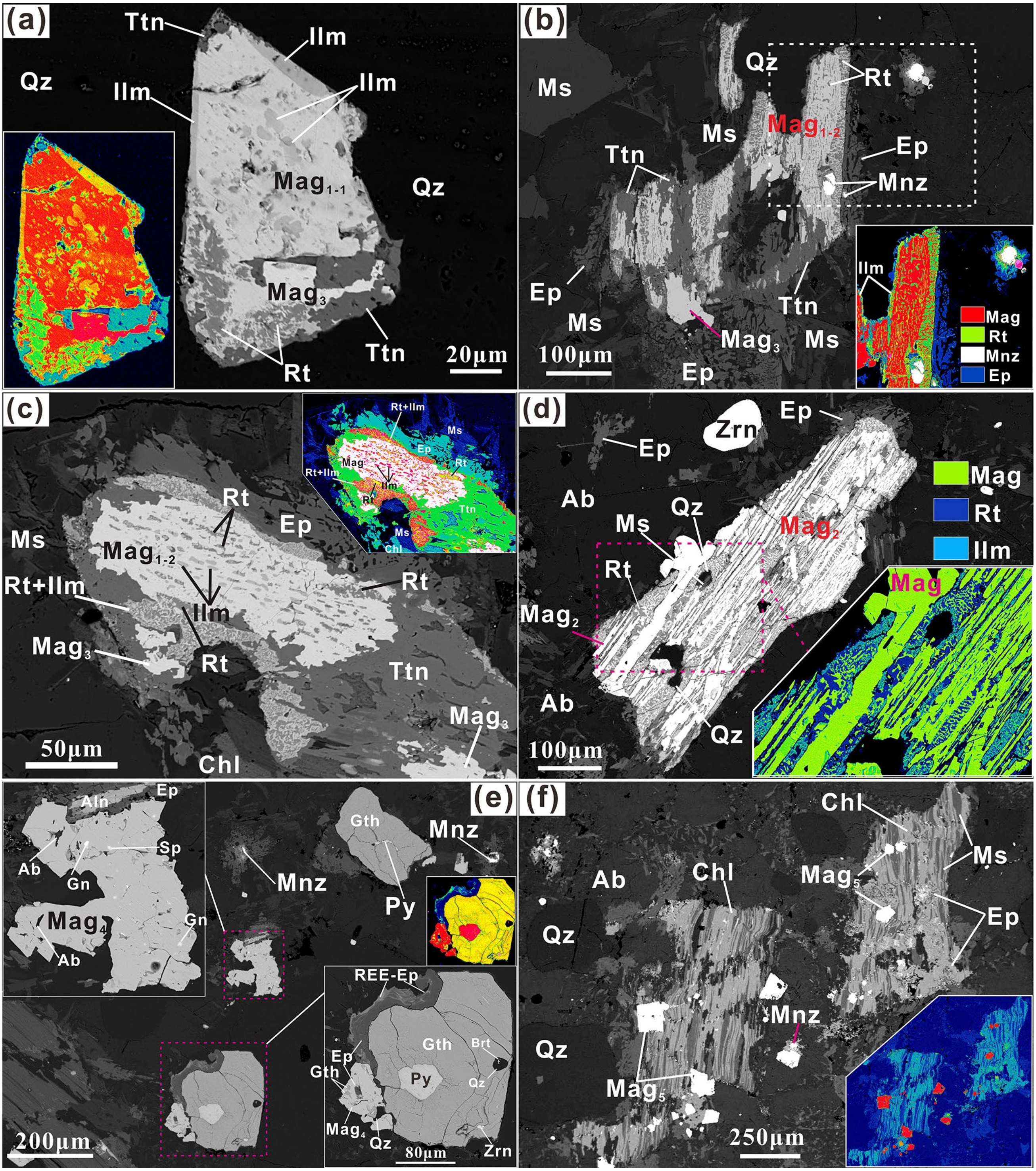

Fig. 7 BSE images showing six types of magnetite in the albitized metagranite. **a** Ilmenite lamellae in the magnetite and ilmenite along the rim of magnetite (Mag_{1-1}). **b** Magnetite (Mag_{1-2}) rimmed by a rutile–magnetite symplectite and locally retrograded to titanite and Mag_3. **c** Magnetite (Mag_{1-2}) with ilmenite and rutile lamellae rimmed by a rutile and ilmenite symplectite and titanite. **d** Rutile and ilmenite intergrowths along the {111} planes in magnetite (Mag_2), which replace the original ilmenite lamellae. **e** Ragged magnetite (Mag_4) with inclusions of galena and sphalerite. **f** Euhedral magnetite (Mag_5) in chloritized muscovite. Mineral abbreviations: *Mag* magnetite, *Ilm* ilmenite, *Ttn* titanite, *Rt* rutile, *Gth* goethite, *Zrn* zircon, *Py* pyrite, *Ttn* titanite, *Gn* galena, *Sp* sphalerite

wt%, respectively. Mag_{1-2} and Mag_2 also show the highest Cr_2O_3 contents. Skeletal-shaped Mag_2 has TiO_2 contents, which range from 0.60 to 1.37 wt% (average 1.14 wt%). Mag_3 exhibits lower TiO_2 contents from 0.25 and 0.97 wt% (average 0.60 wt%). Mag_4 and Mag_5 show similar TiO_2 contents of below 0.2 wt%. Mag_4 also contains NiO. In general, Mag_1 always has the highest Ti V, and Cr contents. Mag_2 has intermediate Ti and Cr contents, while Mag_3 and Mag_4 approximate that of pure Fe_3O_4.

Ilmenite lamellae in magnetite have variable TiO_2 contents ranging from 49.84 to 55.35 wt% ($X_{Ilm} = 0.87–0.98$) and MnO contents ranging from 1.15 to 4.14 wt% ($X_{Pyr} = 0.02–0.08$) (Supplementary Appendix S1, Fig. 7).

Titanite rimming ilmenite–rutile symplectites and the magnetite has FeO, F, and Al_2O_3 contents ranging from 1.11 to 1.71 wt %, 1.04 to 1.21 wt%, and 3.66 to 4.70 wt%, respectively (Supplementary Appendix S1). The Al and Fe content show an inverse correlation with Ti, which is in accordance with the coupled substitution $(Al, Fe)^{3+} + F^- \leftrightarrow Ti^{4+} + O^{2-}$ in the titanite octahedral site (Enami et al. 1993; Fig. 7 and S6b). REE are below the EMP detection limit. The rutile associated with ilmenite and in the symplectite approximate endmember rutile (Supplementary Appendix 1).

Pyrite and goethite

In order to investigate a possible fluid origin for pyrite formation, in situ S isotopic analysis of pyrite in the metagranite were conducted. The pyrites yield $\delta^{34}S_{V\text{-}CDT}$ values ranging from 13.03 ± 0.08‰ to 13.41 ± 0.07‰ (Supplementary Appendix S2). They show a range similar to those from the sillimanite-bearing schist and feldspathic rock in the Liaohe Group (Hao et al. 2017; Sun et al. 2020; Zhao et al. 2009),

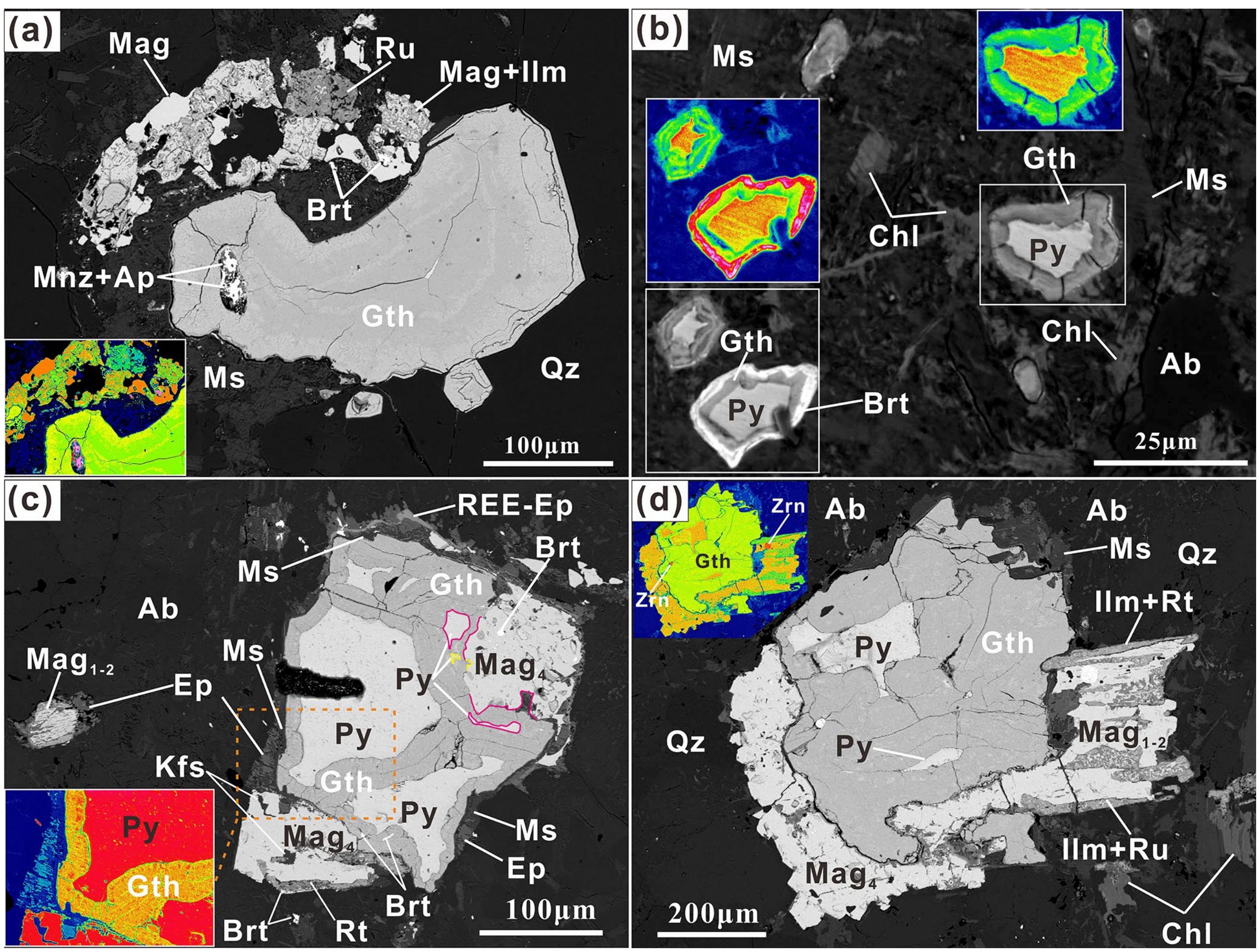

Fig. 8 Representative BSE images showing micro-textures in altered pyrite. **a** Concentric zones of goethite with monazite inclusions, along with the adjoining magnetite. **b** Pyrite surrounded by a goethite corona, which is enclosed by barite. **c** Pyrite partially replaced by goethite along the fractures and rims. The pyrite is associated with magnetite. **d** Pyrite, which is associated with magnetite, has been mostly replaced by goethite. Mineral abbreviations: *Brt* barite

which are interpreted as representing a typical metamorphic signature.

Pyrite in the metagranite is rimmed by goethite with widths of 20–300 µm. In some cases the pyrite has been totally replaced by goethite (Fig. 8a; Supplementary Appendix S1). Some of the goethite shows apparent concentric zoning, and monazite grains can be found as inclusions in the goethite (Fig. 8a). Since goethite has a larger molar volume than that of pyrite, its formation results in radial and concentric micro-fractures (Figs. 7e, 8a, b). Occasionally, in intensively chloritized muscovite, thin barite films may surround the goethite and pyrite (Fig. 8b). Barite crystals are only found near goethite rims around pyrite or as inclusions in Mag_4 (Fig. 8a, b, c). Goethite rims can be surrounded by a 5–20 µm thick layer of muscovite and epidote (Fig. 8c). In addition, some Mag_4 and Mag_{1-2} appears to be intergrown with pyrite, which is being partially replaced by goethite (Fig. 8c, d). Small inclusions of synchysite-(Y) [Ca(Ce, Y)$(CO_3)_2$F] are also found in pyrite (Fig. S7).

Zircon and monazite U–Pb geochronology

In order to date the crystallization and subsequent metasomatic alteration of the metagranite, U–Pb dating of monazite and zircon in the metagranite, and the neighboring monzonite and kyanite-bearing, garnet–sillimanite micaschist were conducted (Fig. 2b; Supplementary Appendix S3). Corresponding U–Pb concordia diagrams and cathodeluminesence (CL) images are shown in Fig. 9.

Under CL imaging, most zircons in the metagranite show distinct zones with bright cores and gray/dark rims (Fig. 9a). From these, 32 CL bright cores with high Th (71–2339 ppm, average 541 ppm) and U contents (32–2336 ppm, average 650 ppm), and Th/U ratios ranging from 0.48 to 1.47, yield $^{207}Pb/^{206}Pb$ ages of 2090 ± 33 to 2239 ± 32 Ma with an upper intercept at 2163 ± 17 Ma (Fig. 9a). This age is interpreted to be the crystallization age of the original granite. In contrast, 19 analyses from the CL dark rims exhibited extremely low Th contents ranging from 8 to 158 ppm, and higher U contents (355–2593 ppm, average 1316 ppm) than those of the CL bright cores, which results in low Th/U ratios of 0.01–0.09. The $^{207}Pb/^{206}Pb$ ages of these CL gray/dark rims are between 1772 and 1880 Ma with an upper intercept at 1849 ± 10 Ma (Fig. 9a).

Monazite grain separates from the metagranite also show distinct compositional zones (Fig. 9b). Thirty-six spot analyses on the BSE dark cores yielded $^{207}Pb/^{206}Pb$ ages of 1902 ± 22–1829 ± 23 Ma with an upper intercept at 1876 ± 36 Ma (MSWD = 0.62). The BSE bright mantles gave $^{207}Pb/^{206}Pb$ ages of 1874 ± 24–1798 ± 26 Ma with an intercept age at 1836 ± 14 Ma (MSWD = 1.10) (Fig. 9b). In addition, the BSE bright mantles exhibit distinct negative Eu anomaly than the BSE dark cores (Fig. 9b).

Zircons from the monzonite show fewer effects from metasomatic alteration and recrystallization. Here the metasomatic rims are narrower than those seen for zircons from the metagranite. The melt crystallization age of the monzonite was obtained from the zircon oscillatory zoned cores using U–Pb dating. A total of 28 dates from the 30 analyzed grains yielded $^{207}Pb/^{206}Pb$ ages from 2251 to 2026 Ma (Fig. 9c), with a weighted mean age of 2166 ± 12 Ma and a Th/U ratio of 0.34–1.15. This age is very close to the presumed crystallization age of the adjoining granite from which the metagranite is derived (2163 ± 17 Ma), which suggests that both the granite and monzonite crystallized at the same time.

The monazites from the monzonite show a bright core and a dark rim in the BSE images (Fig. 9d). Except for six discordant ages, 20 U–Pb dating spots yielded an upper intercept age of 1873 ± 23 Ma (MSWD = 0.88) (Fig. 9d).

Twenty four monazites from the surrounding kyanite-bearing, garnet–sillimanite micaschist give an intercept age of 1869 ± 17 Ma (Fig. 9e). These two sets of dates are nearly identical within the error bars and lie about halfway between the two metamorphic monazite ages for the metagranite suggesting that they may represent a mix of these two ages.

Discussion

Monazite growth and alteration in the metagranite

In the metagranite, the monazite, the Ti–Fe phases, and the plagioclase exhibit features typical of a coupled dissolution–precipitation process. These include a pervasive porosity and extensively developed, fine-grained mineral inclusions in the altered areas of the monazite. These altered areas are delineated from unaltered areas by sharp curved or irregular compositional boundaries (Putnis 2002, 2009; Hetherington and Harlov 2008; Putnis and Austrheim 2010; Harlov et al. 2011; Guillaume et al. 2012; Ruiz-Agudo et al. 2014; Altree-Williams et al. 2015; Grand'Homme et al. 2018).

The complex compositional relationships between different domains in the monazite suggest that monazite growth and fluid alteration occurred simultaneously (Fig. 4). Taking into account the micro-textures, X-ray mapping, geothermometry, and geochronology, we propose that the BSE dark, S-rich monazite cores represent the original monazite the crystallized out with the granite and was later metasomatically altered by a high temperature S-bearing fluid/melt during metamorphism of the granite to a metagranite (Chakhmouradian and Mitchell 1999; Laurent et al. 2016). The BSE bright mantle surrounding the BSE dark magmatic

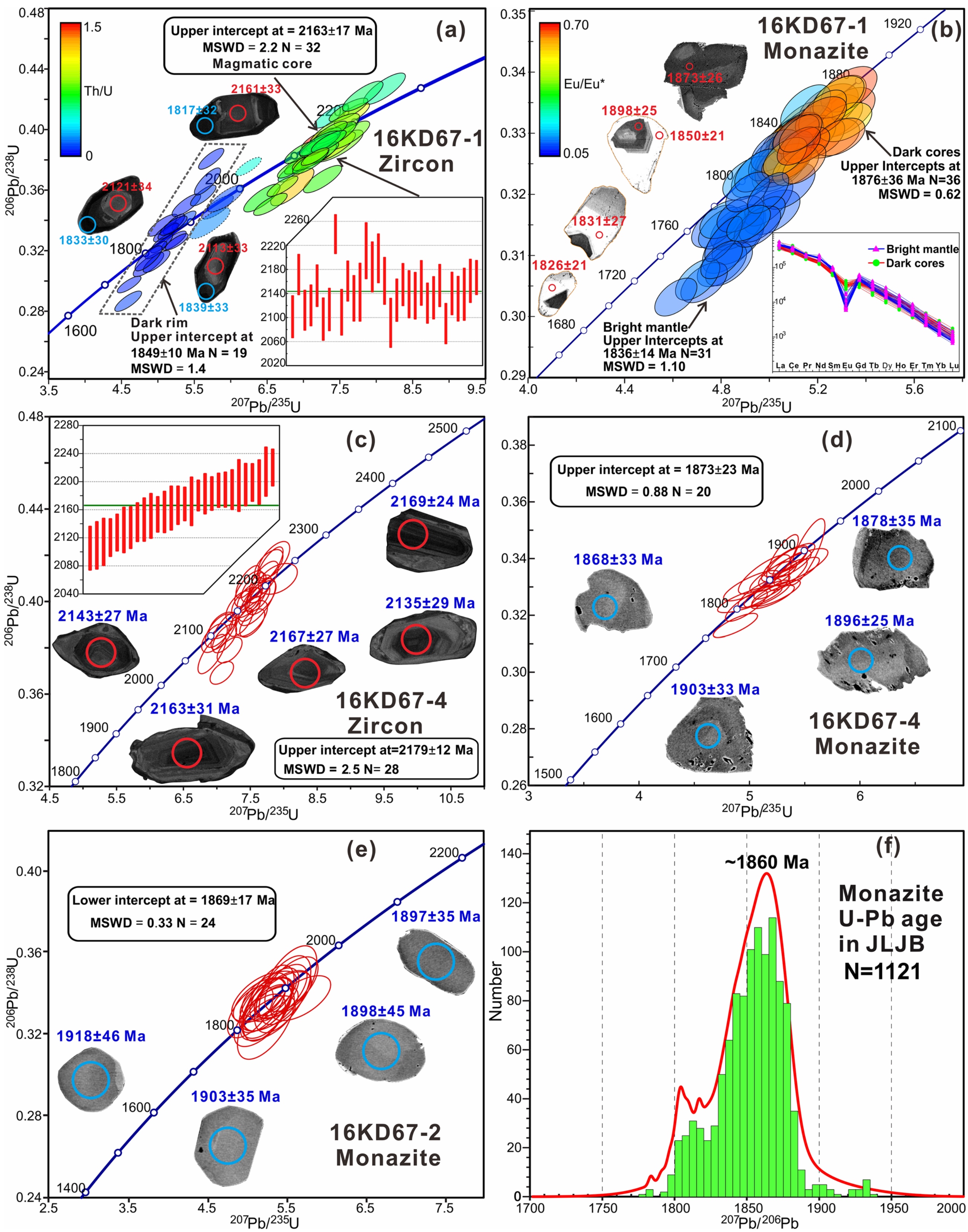
(a)
Upper intercept at = 2163±17 Ma
MSWD = 2.2 N = 32
Magmatic core
16KD67-1
Zircon
Th/U
Dark rim
Upper intercept at
1849±10 Ma N = 19
MSWD = 1.4
2161±33
1817±32
2121±34
1833±30
2113±33
1839±33
(b)
16KD67-1
Monazite
Eu/Eu*
1873±26
1898±25
1850±21
1831±27
1826±21
Dark cores
Upper Intercepts at
1876±36 Ma N=36
MSWD = 0.62
Bright mantle
Upper Intercepts at
1836±14 Ma N=31
MSWD = 1.10
Bright mantle
Dark cores
(c)
16KD67-4
Zircon
Upper intercept at=2179±12 Ma
MSWD = 2.5 N= 28
2169±24 Ma
2143±27 Ma
2167±27 Ma
2135±29 Ma
2163±31 Ma
(d)
Upper intercept at = 1873±23 Ma
MSWD = 0.88 N = 20
1868±33 Ma
1878±35 Ma
1896±25 Ma
1903±33 Ma
16KD67-4
Monazite
(e)
Lower intercept at = 1869±17 Ma
MSWD = 0.33 N = 24
1897±35 Ma
1898±45 Ma
1918±46 Ma
1903±35 Ma
16KD67-2
Monazite
(f)
~1860 Ma
Monazite
U-Pb age
in JLJB
N=1121
Number
207Pb/206Pb
206Pb/238U
207Pb/235U

◂**Fig. 9** $^{206}Pb/^{238}U$ *vs.* $^{207}Pb/^{235}U$ diagram and histogram showing monazite and zircon ages from the JLJ orogenic belt. **a–b** metagranite sample (16KD67-1), Eu/Eu* in **b** referred as $Eu/\sqrt{Sm \times Gd}$. **c–d** monzonite sample (16KD67-4). **e** kyanite-bearing, garnet–sillimanite micaschist (16KD67-2). **f** Age histogram of monazite from JLJ orogenic belt. Representative CL and BSE images and analysis positions are also marked. Red circles represent the initial crystallized age in the melt and the blue circles represent a metamorphic/metasomatic age

core always exhibits an inconsistent orientation with the BSE dark core, such that it sometimes cuts across BSE dark core and concentric zones (Fig. 4a, c), suggesting that the BSE bright mantle must have formed during a subsequent metasomatic/thermal stage, which could have been induced by anatectic veins and S-type granite crystallization in the JLJ orogenic belt from 1870 to 1840 Ma (Liu et al. 2019a). Distinct Eu depletion in the bright mantles compared to BSE dark cores (Fig. 9b) may indicate these areas formed along with Ca-rich minerals and/or fluid infiltration (Kirkland et al. 2016). Following formation of the BSE bright mantle, fluids along fractures in the monazite reacted to form the BSE gray domains along cracks and the BSE gray monazite grain rims (Fig. 4d). Such textures have been reproduced synthetically in experiments involving monazite in which fluid migration occurred along preferential pathways via cracks in the unaltered monazite interior resulting in the alteration of the monazite along these cracks (Harlov et al. 2007, 2011; Budzyn et al. 2011; Williams et al., 2011; Grand'Homme et al. 2018). Sodium-rich fluid alteration of the monazite can result in a decrease in the Ca, Y, and Dy concentrations and an increase in the Th/U ratio in the altered monazite (Grand'Homme et al. 2018), which is consistent with the chemical variation trend seen between the BSE dark core and the BSE bright mantle (Figs. 5 and 10a, b). The irregular BSE light areas in the BSE dark monazite cores may be related to fluid propagation along cracks in the monazite during another metasomatic stage. This is supported by the distinct high UO_2, CaO, and low Nd and Sm contents in these BSE light areas, which plot linearly with the same elements from the BSE dark cores (Fig. 6a, b). When normalized to the average composition of the BSE dark cores (Supplementary Appendix S1; Fig. 10a), a converse LREE variation trend from the concentric zones in the monazite BSE dark core to the BSE bright mantle, BSE gray rim, and, finally, BSE light areas in the core, takes the form of a gradual increase in the Eu_2O_3, SrO, and CaO contents (Supplementary Appendix S1; Fig. 10a). This variation trend most likely occurred during the albitization of the plagioclase by a Na-rich fluid and the release Ca and elements with an affinity for Ca.

Both experimental results and thermodynamic modeling by phase equilibria suggest that the CaO/Na_2O ratio is one of the most crucial parameters controlling whether or not monazite is altered to allanite (Finger et al. 1998; Spear 2010; Budzyń et al. 2011, 2017; Richard et al. 2015). Excess Na in the fluid will prevent the growth of allanite and promote the growth of secondary monazite (Budzyń et al. 2011, 2017). Fluids responsible for the extensive albitization in the plagioclase cores were also responsible for the formation of the high Th and Si and low Ca BSE bright monazite mantles via the huttonitic (Th, U)$SiREE_{-1}P_{-1}$ substitution (Fig. 6a, b) $P^{5+} + (Y^{3+} + REE^{3+}) \leftrightarrow Si^{4+} + Th^{4+}/U^{4+}$ (Zhu et al. 1999; Förster 2006) (Fig. 6a). Calcium released into the fluid during the albitization of the plagioclase permeated the monazite core along micro-fractures to form the BSE light patchy, high Ca and U domains via the cheralitic substitution $2(Y^{3+} + REE^{3+}) \leftrightarrow 2Ca^{2+} + Th^{4+}/U^{4+}$. This Ca-rich fluid may also have helped to initiate the formation of the apatite inclusions occasionally seen in the BSE dark core (Fig. 4b, d). From the BSE dark core to the BSE gray concentric zones to the BSE bright mantle to the BSE gray outer rim the Y_2O_3 and Dy_2O_3 content gradually increases (Figs. 5, 10a), which could also be due in part to an increase in temperature (Heinrich et al. 1997).

In the most likely scenario monazite and zircon crystallized out together at 2160 Ma in the original granitic magma. During the JLJ orogeny at 1960–1800 Ma, the BSE dark core (1902–1870 Ma) was first metasomatized by a S-bearing fluid from the local sulphate-bearing evaporates, such that the monazite geochronometer was reset. During the subsequent isothermal decompression stage (1900–1840 Ma) of the JLJ orogeny, a similar Na-rich fluid originating in the local evaporites induced albitization of the plagioclase, the formation of the monazite BSE bright mantles (1836 ± 14 Ma), and the formation of U and Ca-rich BSE light areas along fractures in the BSE dark cores. Formation of metamorphic rims on the zircon (1849 ± 10 Ma) also occurred at this time. The composition of the altered domains (BSE bright mantles, BSE light areas in the BSE dark cores and pore developed areas) of the monazite shows a distinct compositional decrease of around 1.4–1.5 wt% Y_2O_3 compared to the original monazite (BSE dark core) (Fig. 10b).

Apatite–allanite–epidote coronas around monazite in the metagranite

Apatite–allanite–epidote coronas around monazite are a characteristic alteration texture produced in response to specific *P–T* conditions, local mineral and fluid chemistry, and grain boundary permeabilities. Since Finger et al. (1998) first reported this texture in a granitic gneiss from the eastern Alps, similar textures have been successively found in metagranites (Broska et al. 2005; Budzyń et al. 2010, 2011; Ondrejka et al. 2012; Upadhyay and Pruseth 2012), metasedimentary rocks (Majka and Budzyń 2006; Gasser et al.

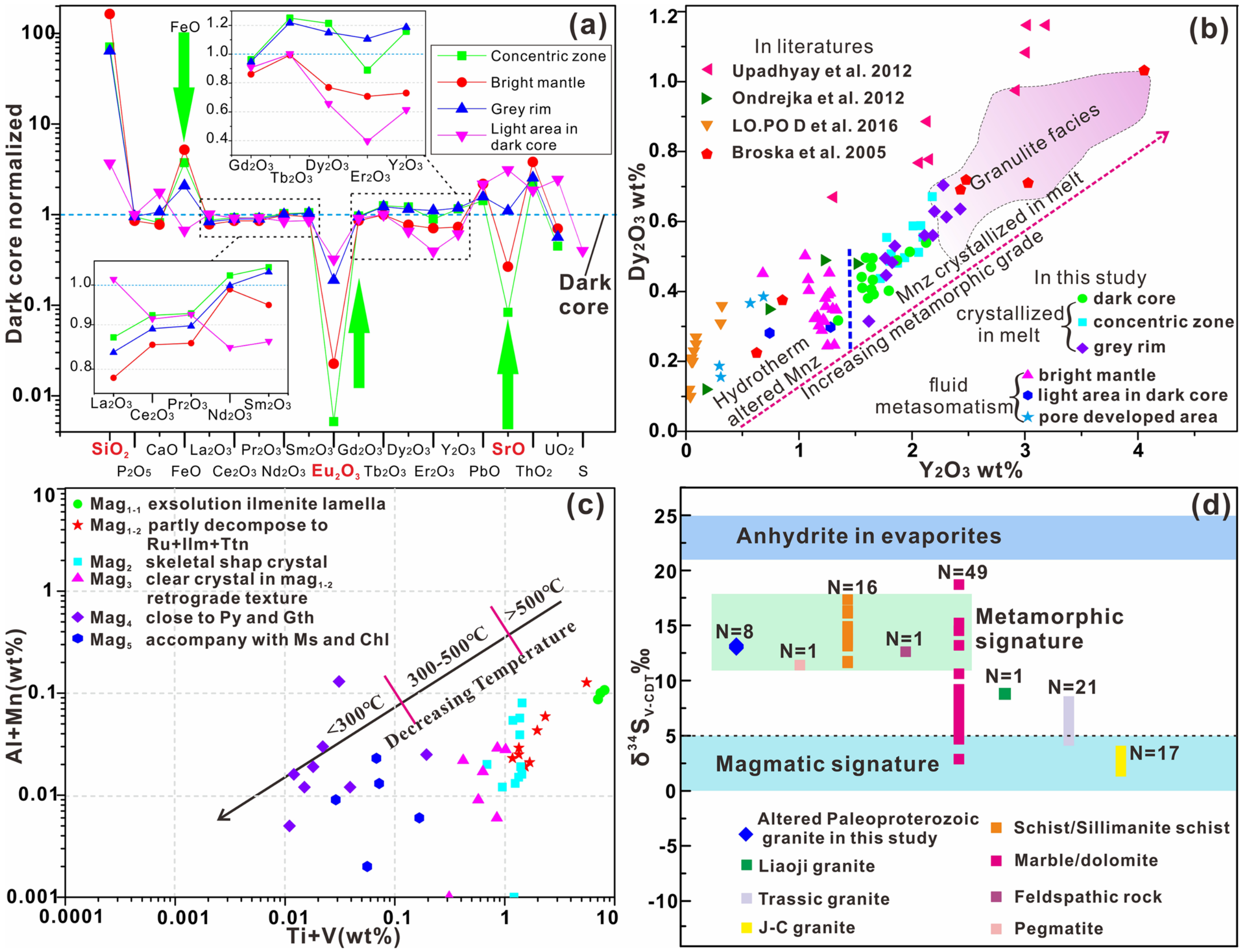

Fig. 10 Analysis diagrams of monazite, magnetite, and pyrite, showing the probable evolutionary process of the magnetite. **a** The average compositional ratios between the BSE gray concentric zone, BSE bright mantle, BSE gray rim, BSE dark cores, and BSE light area in the BSE dark core in the monazite. **b** Y_2O_3 vs. Dy_2O_3 diagram of monazite from the metagranite along with previously reported monazite from apatite–allanite–epidote coronas (Broska et al. 2005; Lo Pò et al. 2016; Ondrejka et al. 2012; Upadhyay and Pruseth 2012). The area for granulite facies monazite is taken from Heinrich et al. (1997). **c** Al + Mn vs. Ti + V diagram (Nadoll et al. 2014a) for the different magnetite types. **d** Sulfur isotopic compositions from the metagranite, the evaporite, and the metamorphic rocks in the Liaohe Group

2012; Lo Pò et al. 2016), and metamorphosed BIF deposits (Xu et al. 2015).

Finger et al. (1998) proposed that this alteration texture formed under amphibolite-facies regional metamorphism and had a relatively slow reaction rate, which was controlled by diffusion, whereas Upadhyay and Pruseth (2012) proposed that the apatite–allanite–epidote corona textures surrounding the monazite were related to high-pressure amphibolite-facies (10–11 kbar and 587–695 °C) fluid-induced retrogression and could be used as a genetic indicator of high-pressure metamorphism. In metasedimentary rocks, these multi-layered coronas associated with monazite can also form under lower *P*–*T* conditions (e.g., greenschist-facies) during either the prograde or retrograde stage (Majka and Budzyń 2006; Rasmussen and Muhling 2007, 2009; Gasser et al. 2012; Lo Pò et al. 2016). Broska et al. (2005) concluded that the fluid-induced alteration and breakdown of monazite partly occurred in response to the alteration of anorthite and biotite. They observed that the breakdown of monazite is more dependent on the fluid composition and the ratio of silicate minerals than on the *P*–*T* conditions, which seems to be the one basic conclusion based on above observations and which is probably the most relevant here in this study.

In the metagranite, the apatite–allanite–epidote corona textures associated with monazite most likely formed as a result of amphibolite-facies metamorphism during the isothermal decompression stage of the JLJ orogeny (1870–1840 Ma) (Liu et al. 2017a, 2019a, b) in the presence of Ca-rich fluids released during the albitization of the plagioclase (Finger et al. 1998; Broska et al. 2005; Ondrejka et al. 2012).

Alteration of oxides and sulphides in the metagranite

Fe–Ti oxides and sulphides are sensitive to changes in the infiltrating fluid chemistry (Hu et al. 2014; Wen et al. 2017) and are crucial indicators of the redox state (Harlov 1992, 2000; Harlov et al. 1997; Harlov and Hansen 2005; Nadoll et al. 2014a; Guo et al. 2017).

The magnetite Ti + V vs. Al + Mn plot of Nadoll et al. (2014a) reveals that $Mag_{1\text{-}2}$, Mag_2, and Mag_3 was altered between 300 and 500 °C (Fig. 10c). This temperature range is consistent with previous temperature estimations for symplectitic rutile formation in a retrograde metabasite (Guo et al. 2017). Mag_4 and Mag_5 formed at temperatures below 300 °C (Fig. 10c). When the Al tetrahedral site (Al^{IV}) chlorite geothermometer (Bourdelle et al. 2013) was applied, it gave late-stage alteration temperatures of 260–310 °C (Supplementary Appendix S1), which coincides with the formation of Mag_4 and Mag_5.

The sulfide minerals from the surrounding country rocks of the Lieryu formation, associated with the metagranite, consist of pervasive gypsum, barite, ludwigite, and anhydrite. Sulfur isotopes from these minerals exhibit a $\delta^{34}S_{V\text{-}CDT}$ value of 20.7 to 24.9 ‰ (Supplementary Appendix S3; Hu et al. 2015a; Peng and Palmer, 2002). In the metagranite, the $\delta^{34}S$ values for pyrite (11.6–17.33 ‰) (Supplementary Appendix S2) are distinctly higher than for a typical magmatic fluid (0–5 ‰) (Chen et al. 2019; Ding et al. 1992; Duan et al. 2017; Li et al. 2019; Liu et al. 2019c; Yu et al. 2018; Zhang et al. 2020). In the marbles and schists from the Liaohe Group, which were metasomatised by a Triassic magmatic fluid, 98% of the pyrites have $\delta^{34}S$ values ranging from 2.8 to 9.1 ‰ with a weighted mean value of 6.8 ‰ (Chi 2002; Duan et al. 2017; Li et al. 2019; Ma et al. 2016; Song et al. 2017). These values are lower than the $\delta^{34}S$ value for pyrite from the metagranite in this study (Fig. 10d). This would suggest that the S in the pyrites from the metagranite was mainly derived from the regional metamorphism of the Lieryu Formation with some contribution from the Liaohe Group.

Integrating together all of these observations, along with the U–Pb ages of the zircon CL gray/dark grain rims and monazite BSE bright mantles (1870–1860 Ma), we propose that the extensive evaporites located in the Lieryu Formation of the Liaohe Group were a crucial external source of Na-, Ba-, Cl-, and SO_4^{2-}-bearing fluids/melts during the high-grade regional metamorphism related to the JLJ orogeny from 1960 to 1900 Ma and subsequent isothermal decompression (1900–1840 Ma) (Peng and Palmer 1995, 2002; Dong et al. 2016, 2017; Hu et al. 2017). These fluids were responsible for the albitization of the original granite to metagranite. The SO_4^{2-} component in these fluids from the evaporites provided a major oxidizing agent, which allowed for the formation of pyrite from pre-existing magnetite (Mag_1 or $Mag_{1\text{-}2}$) in the original granite via the reaction (Li et al. 2014, 2015; Wen et al. 2016):

$$Fe_3O_4 + 6SO_4^{2-} \rightarrow 3FeS_2 + 14O_2. \tag{2}$$

Infiltration of fluids from the evaporite would have coincided with the appearance of fine-grained barite, galena, and/or sphalerite in the vicinity of the pyrite or Mag_4 (Fig. 8b, c). It is also possible from the textures presented in Fig. 8 that some of the pyrite could later have been partially oxidized back to magnetite due to the high oxygen fugacity (Whitney 1984; Harlov et al., 1997; Harlov and Hansen 2005; Drūppel et al. 2006). Finally, the pyrite and magnetite were both partially converted to goethite under high fO_2 and fH_2O conditions during greenschist facies P–T conditions at some later stage.

Geochronology and regional implications

Coupled dissolution–reprecipitation reactions in monazite can induce redistribution of radiogenic Pb and gave rise to meaningless individual dates (Harlov et al. 2011; Williams et al. 2011; Weinberg et al. 2020). Therefore, it can be difficult to distinguish the exact formation age of the monazite core and mantle. Especially, during the post-collision exhumation stage of an orogeny when multiple anatexis and metasomatic events are common (Imayama et al. 2012; Liu et al. 2012; Symington et al. 2014; Poujol et al. 2016; Melo et al. 2017). In JLJ orogenic belt, the ca. 1900 Ma regional tectonic–metamorphic event is well-recognized by many types geochronological dating techniques (Li et al. 2016 and references therein). Especially in the LiaoJi granite (magnetite monzogranite), SHRIMP dating of zircon overgrowth rims yielded a 1914 ± 13 Ma metamorphic age (Li and Zhao 2007). In addition, a compilation of all published monazite ages (N = 1121) of post-tectonic magma and decompression from the JLJ orogenic belt shows more than 78% are located in the range between 1870 and 1800 Ma (Fig. 9f) with a major peak at ca. 1860 Ma. Specific to our study area (Fig. 1c), monazite from a granitoid, a garnet amphibolite, and a metapeltic granulite yield an age range between 1920 and 1820 Ma (Liu et al. 2017b, 2019b), which is interpreted to represent post-peak retrogression. In addition, two zircon age peaks at 1870 Ma and 1840 Ma are also recognized and

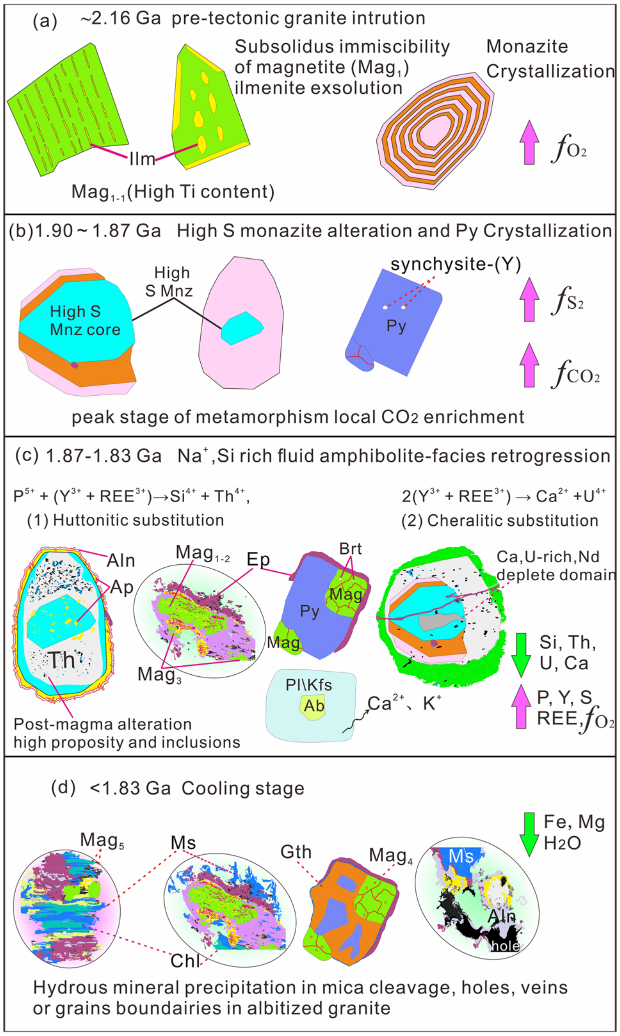

Fig. 11 Schematic illustrations showing the formation, alteration, and breakdown of monazite, magnetite, pyrite, and the related ion exchange reactions in monazite. **a** Oxy-exsolution of ilmenite from the magnetite and monazite crystallization during cooling of the pre-tectonic granite at ~ 2160 Ma. **b** Pyrite and synchysite-(Y) crystallized and pre-existing monazite was metasomatically altered under S- and CO_2-rich conditions during the early stage of the JLJ orogeny (1960–1900 Ma). This occurred when evaporites from the Lieryu Formation of the Liaohe Group underwent extensive partial alteration, which released Na-, Cl-, F-, and SO_4-bearing fluids/melts. **c** During the decompression of the JLJ orogenic belt (1900–1830 Ma), BSE bright mantles formed on the monazite and BSE light areas were metasomatically induced to form in the BSE dark core along cracks. At the same time or shortly after apatite–allanite–epidote coronas formed around the monazite. Ilmenite–rutile–titanite–epidote coronas formed around magnetite from the ilmenite exsolution lamellae in the magnetite. **d** During late stage cooling of the JLJ orogenic belt under approximate greenschist-facies conditions goethite partially replaces pyrite and Ca, K, Fe, Al, and Si are precipitated to form allanite and Mag_5 along chlorite cleavages and fine-grained muscovite around epidote

interpreted to represent two episodes of anatexis (Liu et al. 2017a, 2019a).

Based on the monazite micro-textures in Fig. 4c and the Dy_2O_3 vs Y_2O_3 diagram in Fig. 10b, we speculate that the BSE dark core and gray concentric zone was metasomatically reset during the initial exhumation JLJ orogenic belt at 1900–1870 Ma (Yin and Nie 1996). The BSE bright mantle and gray rim formed during the second episode of anatexis at ~ 1840 Ma both rimming and partly replacing the BSE dark core (Fig. 4c).

Summary

The present results, along with previous investigations, allow us conclude that the evolution of textures associated with monazite, magnetite, and sulphides in the albitized metagranite were a combination of metasomatic processes associated with regional magmatic and metamorphic events (Fig. 11).

Ti-bearing magnetite and monazite crystallized out with the original pre-tectonic granite at ~ 2160 Ma (Fig. 11a). The Ti-bearing magnetite then underwent an ilmenite oxy-exsolution process as the granite cooled allowing for ilmenite lamellae to form in the magnetite. During the high-grade (> 700 °C) regional metamorphic event associated with the JLJ orogeny from 1900 to 1870 Ma, evaporites from the Lieryu Formation of the Liaohe Group underwent extensive partial alteration, which released Na-, Cl-, F-, and SO_4-bearing fluids/melts. This event albitized the pre-tectonic granite to a metagranite while at the same time inducing pyrite to form from pre-existing magnetite (Fig. 11b). A CO_2 component in this fluid induced the formation of synchysite-(Y) inclusions in the pyrite. The original monazite (BSE dark cores and concentric BSE gray oscillatory zone) was metasomatically enriched in S during this time and the geochronometer reset. During exhumation of the JLJ orogenic belt (1870–1830 Ma) (Fig. 11c) BSE bright mantles formed around the monazite and the BSE light areas enriched in Ca and U formed in the BSE dark cores. These, along with the metamorphic rims on zircon, record a fluid-mineral interaction process. During or shortly after this stage, apatite–allanite–epidote coronas formed around monazite and ilmenite–rutile–titanite–epidote coronas formed around magnetite (Mag_1) from the exsolved ilmenite lamellae (Fig. 11c). Concurrent with corona formation, some of pyrite was partly oxidized to Mag_4. Finally, under later greenschist-facies conditions, a decrease in temperature led to LREE, Ca, K, Fe, Al, and Si being precipitated to form allanite and Mag_5 along chlorite cleavages and fine-grained muscovite around epidote, while goethite partly replaced pyrite (Fig. 11d).

Supplementary Information The online version contains supplementary material available at https://doi.org/10.1007/s00410-021-01835-z.

Acknowledgements We thank professor Andrew Putnis, researcher Shuai Guo, Zhonghua Tian, Pinghua Liu and Jia Cai for their helpful discussion. Two anonymous reviewers' constructive comments and reviews are gratefully acknowledged.

Funding This research is funded by the National Natural Science Foundation of China (Projects 92062214, 41890833, 41430210), the Chinese Geological Survey Bureau project (Grant nos. DD20160121) and Basic Scientific Research Foundation of the Institute of Geology, Chinese Academy of Geological Sciences (J2009).

References

Aleinikoff JN, Schenck WS, Plank MO, Srogi L, Fanning CM, Kamo SL, Bosbyshell H (2006) Deciphering igneous and metamorphic events in highgrade rocks of the Wilmington Complex, Delaware: morpholog cathodoluminescence and backscattered electron zoning, and SHRIMP U–Pb geochronology of zircon and monazite. Geol Soc Am Bull 118:39–64. https://doi.org/10.1130/B25659.1

Altree-Williams A, Pring A, Ngothai Y, Brugger J (2015) Textural and compositional complexities resulting from coupled dissolution–reprecipitation reactions in geomaterials. Earth Sci Rev 150:628–651. https://doi.org/10.1016/j.earscirev.2015.08.013

Bourdelle F, Parra T, Chopin C, Beyssac O (2013) A new chlorite geothermometer for diagenetic to low-grade metamorphic conditions. Contrib Miner Petrol 165:723–735

Broska I, Williams CT, Janák M, Nagy G (2005) Alteration and breakdown of xenotime-(Y) and monazite-(Ce) in granitic rocks of the Western Carpathians. Slovakia Lithos 82(1–2):71–83. https://doi.org/10.1016/j.lithos.2004.12.007

Budzyń B, Harlov DE, Kozub-Budzyń GA, Majka J (2017) Experimental constraints on the relative stabilities of the two systems monazite-(Ce)–allanite-(Ce)–fluorapatite and xenotime-(Y)–(Y, HREE)-rich epidote–(Y, HREE)-rich fluorapatite, in high Ca and Na-Ca environments under P–T conditions of 200–1000 MPa and 450–750 °C. Miner Petrol 11:183–217. https://doi.org/10.1007/s00710-016-0464-0

Budzyń B, Harlov DE, Williams ML, Jercinovic MJ (2011) Experimental determination of stability relations between monazite, fluorapatite, allanite, and REE-epidote as a function of pressure, temperature, and fluid composition. Am Mineral 96:1547–1567. https://doi.org/10.2138/am.2011.3741

Budzyń B, Hetherington CJ, Williams ML, Jercinovic MJ, Michalik M (2010) Fluid-mineral interactions and constraints on monazite alterations during metamorphism. Mineral Mag 74(4):633–655

Cai J, Liu FL, Liu PH, Wang F, Meng E, Wang W, Yang H, Ji L, Liu LS (2017) Discovery of granulite-facies metamorphic rocks in the Ji'an area, northeastern Jiao–Liao–Ji Belt, North China Craton: Metamorphic P-T evolution and geological implications. Precambr Res 303:626–640. https://doi.org/10.1016/j.precamres.2017.08.018

Chakhmouradian AR, Mitchell RH (1999) Niobian ilmenite, hydroxylapatite and sulfatian monazite: alternative hosts for incompatible elements in calcite kimberlite from Internatsional'naya, Yakutia. Can Miner 37:1177–1189

Chen C, Li DT, Wu TT, Zhao Y, Zhao CQ, Yang JL, Gu YC (2019) Genesis of gold deposits in the Wulong orefield, Liaodong Peninsula, North China Craton: constraints from ore deposit geology, REE, and C-H–O–S–Pb isotopes. Geol J 55(8):5914–5933. https://doi.org/10.1002/gj.3661

Chen F, Deng J, Wang Q, Huizenga JM, Li G, Gu Y (2020) LA-ICP-MS trace element analysis of magnetite and pyrite from the Hetaoping Fe-Zn-Pb skarn deposit in Baoshan block, SW China: implications for ore-forming processes. Ore Geol Rev. https://doi.org/10.1016/j.oregeorev.2020.103309

Chi YK (2002) Geochemical characteristics of ore-forming elements of the Qingchengzi ore field. J Precious Metallic Geol 11:109–118 **(in Chinese with English abstract)**

Cuney M, Emetz A, Mercadier J, Mykchaylov V, Shunko V, Yuslenko A (2012) Uranium deposits associated with Na-metasomatism from central Ukraine: a review of some of the major deposits and genetic constraints. Ore Geol Rev 44:82–106. https://doi.org/10.1016/j.oregeorev.2011.09.007

Ding TP, Jiang SY, Wan DF, Li JC, Song B, Zhao DM (1992) Stable Isotope Studies on the Proterozoic Pb-Zn Mineral Belt of northern China. Beijing Publishing House of Science and Technology, Beijing

Dong AG, Zhu XK, Li SZ, Kendall B, Wang Y, Gao ZF (2016) Genesis of a giant Paleoproterozoic strata-bound magnesite deposit: constraints from Mg isotopes. Precambr Res 281:673–683. https://doi.org/10.1016/j.precamres.2016.06.020

Dong AG, Zhu XK, Li ZH, Kendall B, Li SZ, Wang Y, Tang C (2017) A multi-isotope approach towards constraining the origin of large-scale Paleoproterozoic B-(Fe) mineralization in NE China. Precambr Res 292:115–129. https://doi.org/10.1016/j.precamres.2017.01.030

Drūppel K, Wagner T, Boyce AJ (2006) Evolution of sulfide mineralization in ferrocarbonatite, Swartbooidsrif, NW Namibia: constraints from mineral chemistry and sulfur isotopes. Can Miner 44(4):877–894

Duan XX, Zeng QD, Wang YB, Zhou LL, Chen B (2017) Genesis of the Pb−Zn deposits of the Qingchengzi ore field, eastern Liaoning, China: constraints from carbonate LA−ICPMS trace element analysis and C-O–S–Pb isotopes. Ore Geol Rev 89:752–771. https://doi.org/10.1016/j.oregeorev.2017.07.012

Enami M, Suzuki K, Liou J, Bird DK (1993) Al-Fe^{3+} and F–OH substitutions in titanite and constraints on their P-T dependence. Eur J Mineral 5(2):219–231. https://doi.org/10.1127/EJM/5/2/0219

Finger F, Broska I, Roberts MP, Schermaier A (1998) Replacement of primary monazite by apatite-allanite-epidote coronas in an amphibolite facies granite gneiss from the eastern Alps. Am Mineral 83:248–258. https://doi.org/10.2138/am-1998-3-408

Förster HJ (2006) Composition and origin of intermediate solid solutions in the system thorite-xenotime-zircon-coffinite. Lithos 88(1–4):35–55. https://doi.org/10.1016/j.lithos.2005.08.003

Fu JL, Hu ZC, Zhang W, Yang L, Liu YS, Li M, Zong KQ, Gao S, Hu SH (2016) In situ, sulfur isotopes ($\delta^{34}S$ and $\delta^{33}S$) analyses in sulfides and elemental sulfur using high sensitivity cones combined with the addition of nitrogen by Laser Ablation MC-ICP-MS. Anal Chim Acta 911:14–26. https://doi.org/10.1016/j.aca.2016.01.026

Gasser D, Bruand E, Rubatto D, Stuwe K (2012) The behaviour of monazite from greenschist facies phyllites to anatectic gneisses: an example from the Chugach Metamorphic Complex, southern Alaska. Lithos 134–135(3–3):108–122. https://doi.org/10.1016/j.lithos.2011.12.003

Grand'Homme A, Janots E, Seydoux-Guillaume AM, Guillaume D, Magnin V, Hövelmann J, Höschen C, Boiron MC (2018) Mass transport and fractionation during monazite alteration by anisotropic replacement. Chem Geol 484:51–68. https://doi.org/10.1016/j.chemgeo.2017.10.008

Gratz R, Heinrich W (1997) Monazite–xenotime thermobarometry: experimental calibration of the miscibility gap in the system

$CePO_4$–YPO_4. Am Mineral 82:772–780. https://doi.org/10.2138/am-1997-7-816
Gratz R, Heinrich W (1998) Monazite–xenotime thermometry. III. Experimental calibration of the partitioning of gadolinium between monazite and xenotime. Eur J Mineral 10:579–588. https://doi.org/10.1127/ejm/10/3/0579
Guillaume AMS, Montel JM, Bingen B, Bosse V, Parseval P, Paquette JL, Janots E, Wirth R (2012) Low-temperature alteration of monazite: fluid mediated coupled dissolution–precipitation, irradiation damage, and disturbance of the U–Pb and Th–Pb chronometers. Chem Geol 330–331:140–158. https://doi.org/10.1016/j.chemgeo.2012.07.031
Guo S, Tang P, Su B, Chen Y, Ye K, Zhang L, Gao Y, Liu J, Yang Y (2017) Unusual replacement of Fe-Ti oxides by rutile during retrogression in amphibolite-hosted veins (Dabie UHP terrane): a mineralogical record of fluid-induced oxidation processes in exhumed UHP slabs. Am Mineral 102:2268–2283. https://doi.org/10.2138/am-2017-6120
Hao LB, Zhao X, Zhao YY (2017) Stable isotope characteristics and ore genesis of the Baiyun gold deposit Liaoning province. J Jilin Univ 47:442–451
Harlov DE (1992) Comparative oxygen barometry in granulites, bamble sector. SE Norway J Geo 100(4):446–467. https://doi.org/10.1086/629597
Harlov DE (2000) Titaniferous magnetite-ilmenite thermometry and titaniferous magnetite-ilmenite-orthopyroxene-quartz oxygen barometry in granulite facies gneisses, Bamble Sector, SE Norway: implications for the role of high-grade CO_2-rich fuids during granulite genesis. Contrib Mineral Petrol 1139:180–197. https://doi.org/10.1007/PL00007670
Harlov DE, Hansen EC (2005) Oxide and sulphide isograds along a late Archean, deep-crustal profile in Tamil Nadu, south India. J Metam Geol 23:241–259
Harlov DE, Hetherington CJ (2010) Partial high-grade alteration of monazite using alkali-bearing fluids: experiment and nature. Am Mineral 95(7):1105–1108. https://doi.org/10.2138/am.2010.3525
Harlov DE, Newton RC, Hansen EC, Jarnardhan AS (1997) Oxide and sulphide minerals in highly oxidized Rb-depleted Archean granulites of the Shevaroy Hills Massif, South India: oxidation states and the role of metamorphic fluids. J Metamorph Geol 15:701–717
Harlov DE, Wirth R, Förster HJ (2005) An experimental study of dissolution-reprecipitation in fluorapatite: fluid infiltration and the formation of monazite. Contrib Miner Petrol 150(3):268–286. https://doi.org/10.1007/s00410-005-0017-8
Harlov DE, Wirth R, Hetherington CJ (2007) The relative stability of monazite and huttonite at 300–900 °C and 200–1000 MPa: metasomatism and the propagation of metastable mineral phases. Am Mineral 92(10):1652–1664. https://doi.org/10.2138/am.2007.2459
Harlov DE, Wirth R, Hetherington CJ (2011) Fluid-mediated partial alteration of monazite: the role of fluids during apparent solid state element mass transfer. Contrib Mineral Petrol 162:329–348. https://doi.org/10.1007/s00410-010-0599-7
Heinrich W, Andrehs G, Franz G (1997) Monazite–xenotime miscibility gap thermometry I An empirical calibration. J Metamorph Geol 15(1):3–16. https://doi.org/10.1111/j.1525-1314.1997.t01-1-00052.x
Hetherington CJ, Harlov DE (2008) Metasomatic thorite and uraninite inclusions in xenotime and monazite from granitic pegmatites, Hidra anorthosite massif, southwestern Norway: mechanics and fluid chemistry. Am Mineral 93:806–820. https://doi.org/10.2138/am.2008.2635
Hetherington CJ, Harlov DE, Budzyń B (2010) Experimental metasomatism of monazite and xenotime: mineral stability, REE mobility and fluid composition. Mineral Petrol 99:165–184. https://doi.org/10.1007/s00710-010-0110-1
Horstwood MSA, Foster GL, Parrish RR, Noble SR, Nowell GM (2003) Common-Pb corrected in situ U-Pb accessory mineral geochronology by LAMC-ICP-MS. J Anal at Spectrom 18:837–846. https://doi.org/10.1039/B304365G
Hu GY, Li YH, Fan CF, Hou KJ, Zhao Y, Zeng LS (2015a) In situ LA–MC–ICP–MS boron isotope and zircon U-Pb age determinations of Paleoproterozoic borate deposits in Liaoning Province, northeastern China. Ore Geol Rev 65:1127–1141. https://doi.org/10.1016/j.oregeorev.2014.09.005
Hu H, Lentz D, Li JW, McCarron T, Zhao XF, Hall D (2015b) Reequilibration processes in magnetite from iron skarn deposits. Econ Geol 110(1):1–8. https://doi.org/10.2113/econgeo.110.1.1
Hu H, Li JW, Lentz D, Ren Z, Zhao XF, Deng XD, Hall D (2014) Dissolution–reprecipitation process of magnetite from the Chengchao iron deposit: insights into ore genesis and implication for in-situ chemical analysis of magnetite. Ore Geol Rev 57:393–405. https://doi.org/10.1016/j.oregeorev.2013.07.008
Hu X, Chen H, Zhao L, Han J, Xia X (2017) Magnetite geochemistry of the Longqiao and Tieshan Fe–(Cu) deposits in the Middle-Lower Yangtze River Belt: implications for deposit type and ore genesis. Ore Geol Rev 89:822–835. https://doi.org/10.1016/j.oregeorev.2017.07.019
Hu ZC, Gao S, Liu YS, Hu SH, Chen HH, Yuan HL (2008) Signal enhancementin laser ablation ICP-MS by addition of nitrogen in the central channel gas. J Anal at Spectrom 23(3):1093–1101. https://doi.org/10.1039/b804760j
Hu ZC, Zhang W, Liu YS, Gao S, Li M, Zong KQ, Chen HH, Hu SH (2015c) "Wave" signal-smoothing and mercury-removing device for laser ablation quadrupole and multiple collector icpms analysis: application to lead isotope analysis. Anal Chem 87(2):1152–1157. https://doi.org/10.1021/ac503749k
Imayama T, Takeshita T, Yi K, Cho D-L, Kitajima K, Tsutsumi Y, Kayama M, Nishido H, Okumura T, Yagi K, Itaya T, Sano Y (2012) Two-stage partial melting and contrasting cooling history within the higher himalayan crystalline sequence in the far-eastern Nepal Himalaya. Lithos 134–135:1–22. https://doi.org/10.1016/j.lithos.2011.12.004
Itano K, Iizuka T, Chang Q, Kimura JI, Maruyama S (2016) U–Pb chronology and geochemistry of detrital monazites from major African rivers: constraints on the timing and nature of the Pan-African Orogeny. Precambr Res 282:139–156. https://doi.org/10.1016/j.precamres.2016.07.008
Jamtveit B, Malthesorenssen A, Kostenko O (2008) Reaction enhanced permeability during retrogressive metamorphism. Earth Planet Sci Lett 267(3–4):620–627. https://doi.org/10.1016/j.epsl.2007.12.016
Jiang SY, Palmer MR, Peng QM, Yang JH (1997) Chemical and stable isotopic compositions of Proterozoic metamorphosed evaporites and associated tourmalines from the Houxianyu borate deposit, eastern Liaoning. China Chem Geol 135(3–4):189–211. https://doi.org/10.1016/S0009-2541(96)00115-5
Kelsey DE, Clark C, Hand M (2008) Thermobarometric modelling of zircon and monazite growth in melt-bearing systems: examples using model metapelitic and metapsammitic granulites. J Metamorph Geol 26(2):199–212. https://doi.org/10.1111/j.1525-1314.2007.00757.x
Kimura JI, Chang Q, Tani K (2011) Optimization of ablation protocol for 200 nm UV femtosecond laser in precise U–Pb age dating coupled to multi-collector ICP mass spectrometry. Geochem J 45:283–296. https://doi.org/10.2343/geochemj.1.0120
Kirkland CL, Erickson TM, Johnson TE, Danišík M, Evans NJ, Bourdet J, McDonald BJ (2016) Discriminating prolonged, episodic or disturbed monazite age spectra: an example from the Kalak

Nappe Complex, Arctic Norway. Chem Geol 424:96–110. https://doi.org/10.1016/j.chemgeo.2016.01.009
Laurent AT, Seydoux-Guillaume A-M, Duchene S, Bingen B, Bosse V, Datas L (2016) Sulphate incorporation in monazite lattice and dating the cycle of sulphur in metamorphic belts. Contrib Mineral Petrol. https://doi.org/10.1007/s00410-016-1301-5
Li J, Cai WY, Li B, Wang KY, Liu HL, Konare Y, Qian Y, Lee GJ, Yoo BC (2019) Paleoproterozoic SEDEX type stratiform mineralization overprinted by Mesozoic vein-type mineralization in the Qingchengzi Pb Zn deposit Northeastern China. J of Asian Earth Sci. https://doi.org/10.1016/j.jseaes.2019.104009
Li SZ, Zhao GC (2007) SHRIMP U-Pb zircon geochronology of the Liaoji granitoids: constraints on the evolution of the Paleoproterozoic Jiao-Liao-Ji belt in the Eastern Block of the North China Craton. Precambr Res 158(1–2):1–16. https://doi.org/10.1016/j.precamres.2007.04.001
Li SZ, Zhao GC, Sun M, Han ZZ, Luo Y, Hao DF, Xia XP (2005) Deformation history of the Paleoproterozoic Liaohe assemblage in the eastern block of the North China Craton. J Asian Earth Sci 24(5):659–674. https://doi.org/10.1016/j.jseaes.2003.11.008
Li WT, Audétat A, Zhang J (2015) The role of evaporites in the formation of magnetite–apatite deposits along the Middle and Lower Yangtze River, China: evidence from LA-ICP-MS analysis of fluid inclusions. Ore Geol Rev 67:264–278
Li YH, Duan C, Han D, Chen XW, Wang CL, Yang BY, Zhang C, Liu F (2014) Effect of sulfate evaporate salt layer for formation of porphyrite iron ores in the Middle-Lower Yangtze River area. Acta Petrol Sin 30:1355–1368 **(in Chinese with English abstract)**
Li Z, Chen B, Wei CJ (2017) Is the Paleoproterozoic Jiao-Liao-Ji Belt (North China Craton) a rift? Int J Earth Sci 106:355–375. https://doi.org/10.1007/s00531-016-1323-2
Liu FL, Liu CH, Itano K, Iizuka T, Cai J, Wang F (2017a) Geochemistry, U–Pb dating, and Lu–Hf isotopes of zircon and monazite of porphyritic granites within the Jiao-Liao-Ji orogenic belt: implications for petrogenesis and tectonic setting. Precambr Res 300:78–106. https://doi.org/10.1016/j.precamres.2017.08.007
Liu FL, Liu LS, Cai J, Liu PH, Wang F, Liu CH, Liu JH (2019a) A widespread Paleoproterozoic partial melting event within the Jiao-Liao-Ji Belt, North China Craton: zircon U-Pb dating of granitic leucosomes within pelitic granulites and its tectonic implications. Precambr Res 326:155–173. https://doi.org/10.1016/j.precamres.2017
Liu FL, Robinson PT, Liu PH (2012) Multiple partial melting events in the Sulu UHP terrane: zircon U-Pb dating of granitic leucosomes within amphibolite and gneiss. J Metam Geol 30(8):887–906. https://doi.org/10.1111/j.1525-1314.2012.01005.x
Liu J, Zhang LJ, Wang SL, Li TG, Yang Y, Liu FX, Li SH, Duan C (2019b) Formation of the Wulong gold deposit, Liaodong gold Province, NE China: constraints from zircon U-Pb age, sericite Ar–Ar age, and H–O–S–He isotopes. Ore Geol Rev 109:130–143. https://doi.org/10.1016/j.oregeorev.2019.04.013
Liu PH, Cai J, Zou L (2017b) Metamorphic P-T-t path and its geological implications of the Sanjiazi garnet amphibolites from the northern Liaodong Penisula, Jiao-Liao-Ji belt: constraints on phase equilibria and zircon U–Pb dating. Acta Petrol Sin 33(9):2649–2674 **(in Chinese with English abstract)**
Liu PH, Liu FL, Tian ZH, Cai J, Ji L, Wang F (2019c) Petrological and geochronological evidence for Paleoproterozoic granulite-facies metamorphism of the South Liaohe Group in the Jiao-Liao-Ji Belt, North China Craton. Precambr Res 327:121–143. https://doi.org/10.1016/j.precamres.2019.03.002
Lo Pò D, Braga R, Massonne HJ, Molli G, Montanini A, Theye T (2016) Fluid-induced breakdown of monazite in medium-grade metasedimentary rocks of the Pontremoli basement (Northern Apennines, Italy). J Metamorph Geol 34:63–84
Lu XP, Wu FY, Guo JH, Wilde SA, Yang JH, Liu XM, Zhang XO (2006) Zircon U-Pb geochronological constraints on the Paleoproterozoic crustal evolution of the Eastern block in the North China Craton. Precambr Res 146(3–4):138–164. https://doi.org/10.1016/j.precamres.2006.01.009
Liu YS, Gao S, Hu ZC, Gao CG, Zong KQ, Wang DB (2010) Continental and oceanic crust recycling-induced melt-peridotite interactions in the Trans-North China Orogen: U-Pb dating, Hf isotopes and trace elements in zircons of mantle xenoliths. J Petrol 51(1–2):537–571. https://doi.org/10.1093/petrology/egp082
Ludwig KR (2003) User's Manual for Isoplot/EX Version 3.00. A Geochronological Toolkit for Microsoft Excel. Berkeley Geochronology Center Special Publication
Ma YB, Bagas L, Xing SW, Zhang ST, Wang RJ, Li N, Zhang ZJ, Zou YF, Yang XQ, Wang Y, Zhang Y (2016) Genesis of the stratiform Zhenzigou Pb Zn deposit in the North China Craton: Rb Sr and C O S Pb isotope constraints. Ore Geol Rev 79:88–104. https://doi.org/10.1016/j.oregeorev.2016.05.009
Majka J, Budzyń B (2006) Monazite breakdown in metapelites from Wedel Jarlsberg Land Svalbard preliminary report. Mineral Pol 37(1):61–68. https://doi.org/10.2478/v10002-007-0006-9
Melo MG, Stevens G, Lana C, Pedrosa-Soares AC, Frei D, Alkmim FF, Alkmin LA (2017) Two cryptic anatectic events within a syn-collisional granitoid from the Araçuaí orogen (southeastern Brazil): evidence from the polymetamorphic Carlos Chagas batholith. Lithos 277:51–71. https://doi.org/10.1016/j.lithos.2016.10.012
Misch D, Pluch H, Mali H, Ebner F, Huang H (2018) Genesis of giant Early Proterozoic magnesite and related talc deposits in the Mafeng area, Liaoning Province, NE China. J Asian Earth Sci 160:1–12. https://doi.org/10.1016/j.jseaes.2018.04.005
Nadoll P, Angerer T, Mauk JL, French D, Walshe J (2014a) The chemistry of hydrothermal magnetite: a review. Ore Geol Rev 61:1–32. https://doi.org/10.1016/j.oregeorev.2013.12.013
Nadoll P, Mauk JL, Hayes TS, Koenig AE, Box SE (2012) Geochemistry of magnetite from hydrothermal ore deposits and host rocks of the Mesoproterozoic Belt Supergroup. United States Econ Geol 107(6):1275–1292. https://doi.org/10.2113/econgeo.107.6.1275
Nadoll P, Mauk JL, Leveille RA, Koenig AE (2014b) Geochemistry of magnetite from porphyry Cu and skarn deposits in the southwestern United States. Mineral Deposita 50:493–515. https://doi.org/10.1007/s00126-014-0539-y
Ondrejka M, Uher P, Putiš M, Broska I, Bačík P, Konečný P, Schmiedt I (2012) Two-stage breakdown of monazite by post-magmatic and metamorphic fluids: an example from the Veporic orthogneiss, Western Carpathians, Slovakia. Lithos 142–143:245–255. https://doi.org/10.1016/j.lithos.2012.03.012
Parrish RR (1990) U–Pb dating of monazite and its application to geological problems. Can J Earth Sci 27:1435–1450. https://doi.org/10.1139/e90-152
Peng QM, Palmer MR (1995) The Palaeoproterozoic boron deposits in eastern Liaoning China: a metamorphosed evaporate. Precambr Res 72(3–4):185–197. https://doi.org/10.1016/0301-9268(94)00087-8
Peng QM, Palmer MR (2002) The paleoproterozoic Mg and Mg–Fe borate deposits of Liaoning and Jilin provinces. Northeast China Econ Geol 97(1):93–108. https://doi.org/10.2113/gsecongeo.97.1.93
Poujol M, Pitra P, Van Den Driessche J, Tartèse R, Ruffet G, Paquette J-L, Poilvet J-C (2016) Two-stage partial melting during the Variscan extensional tectonics (Montagne Noire, France). Int J Earth Sci 106(2):477–500. https://doi.org/10.1007/s00531-016-1369-1
Putnis A (2002) Mineral replacement reactions: from macroscopic observations to microscopic mechanisms. Mineral Mag 66:689–708

Putnis A (2009) Mineral replacement reactions. Rev Mineral Geochem 70(1):87–124. https://doi.org/10.2138/rmg.2009.70.3

Putnis A, Austrheim H (2010) Fluid induced processes: metasomatism and metamorphism. Geofluids 10:254–269. https://doi.org/10.1111/j.1468-8123.2010.00285.x

Pyle JM, Spear FS, Rudnick RL, McDonough WF (2001) Monazite–xenotime–garnet equilibrium in metapelites and a new monazite–garnet thermometer. J Petrol 42(11):2083–2107. https://doi.org/10.1093/petrology/42.11.2083

Rasmussen B, Muhling JR (2007) Monazite begets monazite: evidence for dissolution of detrital monazite and reprecipitation of syntectonic monazite during low-grade regional metamorphism. Contrib Mineral Petrol 154(6):675–689. https://doi.org/10.1007/s00410-007-0216-6

Rasmussen B, Muhling JR (2009) Reactions destroying detrital monazite in greenschist-facies sandstones from the Witwatersrand basin. South Africa Chem Geol 264(1–4):311–327. https://doi.org/10.1016/j.chemgeo.2009.03.017

Richard A, Montel J-M, Leborgne R, Peiffert C, Cuney M, Cathelineau M (2015) Monazite alteration in $H_2O \pm HCl \pm NaCl \pm CaCl_2$ fluids at 150 °C and psat: implications for uranium deposits. Minerals 5(4):693–706. https://doi.org/10.3390/min5040518

Ruiz-Agudo E, Putnis CV, Putnis A (2014) Coupled dissolution and precipitation at mineral–fluid interfaces. Chem Geol 383:132–146. https://doi.org/10.1016/j.chemgeo.2014.06.007

Shrestha S, Larson KP, Duesterhoeft E, Soret M, Cottle JM (2019) Thermodynamic modelling of phosphate minerals and its implications for the development of P-T-t histories: a case study in garnet–monazite bearing metapelites. Lithos 334–335:141–160. https://doi.org/10.1016/j.lithos.2019.03.021

Simonetti A, Heaman LM, Chacko T, Banerjee NR (2006) In situ petrographic thin section U–Pb dating of zircon, monazite, and titanite using laser ablation–MC–ICP-MS. Int J Mass Spectrom 253:87–97. https://doi.org/10.1016/j.ijms.2006.03.003

Song YH, Yang FC, Yan GL, Wei MH, Shi SS (2017) Characteristics of mineralization fluids and tracers of mineralization material sources of the Qingchengzi lead-zinc deposit in Liaoning Province. Geol Explor 53(2):0259–0269 **(in Chinese with English abstract)**

Spear FS (2010) Monazite–allanite phase relations in metapelites. Chem Geol 279(1–2):55–62. https://doi.org/10.1016/j.chemgeo.2010.10.004

Stepanov AS, Rubatto HJ, RappRP D (2012) Experimental study of monazite/melt partitioning with implications for the REE, Th and U geochemistry of crustal rocks. Chem Geol 300–301:200–220. https://doi.org/10.1016/j.chemgeo.2012.01.007

Sun GT, Zeng QD, Zhou LL, Wang YB, Chen PW (2020) Trace element contents and in situ sulfur isotope analyses of pyrite in the Baiyun gold deposit, NE China: implication for the genesis of intrusion-related gold deposits. Ore Geol Rev. https://doi.org/10.1016/j.oregeorev.2020.103330

Symington NJ, Weinberg RF, Hasalova P, Wolfram LC, Raveggi M, Armstrong RA (2014) Multiple intrusions and remelting-remobilization events in a magmatic arc The St. Peter Suite South Australia. Geol Soc Am Bull 126:1200–1218. https://doi.org/10.1130/b30975.1

Tam PY, Zhao GC, Liu FL, Zhou XW, Sun M, Li SZ (2011) Timing of metamorphism in the paleoproterozoic Jiao-Liao-Ji Belt: New SHRIMP U–Pb zircon dating of granulites, gneisses and marbles of the Jiaobei massif in the North China Craton. Gondwana Res 19:150–162. https://doi.org/10.1016/j.gr.2010.05.007

Tam PY, Zhao GC, Sun M, Li SZ, Iizuka Ki Ma YGS, Yin CQ, He YH, Wu ML (2012a) Metamorphic P–T path and tectonic implications of medium-pressure pelitic granulites from the Jiaobei massif in the Jiao-Liao-Ji Belt, North China Craton. Precambr Res 220–221:177–191. https://doi.org/10.1016/j.precamres.2012.08.008

Tam PY, Zhao GC, Sun M, Li SZ, Wu ML, Yin CQ (2012b) Petrology and metamorphic P–T path of high-pressure mafic granulites from the Jiaobei massif in the Jiao-Liao-Ji Belt, North China Craton. Lithos 155:94–109. https://doi.org/10.1016/j.lithos.2012.08.018

Tam PY, Zhao GC, Zhou X, Sun M, Guo JH, Li S, Yin CQ, Wu ML, He YH (2012c) Metamorphic P–T path and implications of high-pressure pelitic granulites from the Jiaobei massif in the Jiao-Liao-Ji Belt. North China Craton Gondwana Res 22(1):104–117. https://doi.org/10.1016/j.gr.2011.09.006

Tian ZH, Liu FL, Windley BF, Liu PH, Wang F, Liu CH, Wang W, Cai J, Xiao WJ (2017) Polyphase structural deformation of low- to medium-grade metamorphic rocks of the Liaohe Group in the Jiao-Liao-Ji Orogenic Belt, North China Craton: correlations with tectonic evolution. Precambr Res 303:641–659. https://doi.org/10.1016/j.precamres.2017.08.017

Upadhyay D, Pruseth KL (2012) Fluid-induced dissolution breakdown of monazite from TsoMorari complex, NW Himalayas: evidence for immobility of trace elements. Contrib Mineral Petrol 164:303–316. https://doi.org/10.1007/s00410-012-0739-3

Wan YS, Song B, Liu DY, Wilde SA, Wu JS, Shi YL, Yin XY, Zhou HY (2006) SHRIMP U–Pb zircon geochronology of Paleoproterozoic metasedimentary rocks in the North China Craton: evidence for a major late paleoproterozoic tectonothermal event. Precambr Res 149(3–4):249–271. https://doi.org/10.1016/j.precamres.2006.06.006

Wang AJ, Peng QM, Palmer MR (1998) Salt dome-controlled sulfide precipitation of paleoproterozoic Fe–Cu sulfide deposits eastern Liaoning Northeastern China. Econ Geol 93:1–14. https://doi.org/10.2113/gsecongeo.93.1.1

Wang F, Liu FL, Liu PH, Cai J, Schertl HP, Ji L, Liu LS, Tian ZH (2017) In situ zircon U–Pb dating and whole-rock geochemistry of metasedimentary rocks from South Liaohe Group, Jiao-Liao-Ji orogenic belt: constraints on the depositional and metamorphic ages, and implications for tectonic setting. Precambr Res 303:764–780. https://doi.org/10.1016/j.precamres.2017.10.002

Weinberg RF, Wolfram LC, Nebel O, Hasalová P, Závada P, Kylander-Clark ARC, Becchio R (2020) Decoupled U-Pb date and chemical zonation of monazite in migmatites: the case for disturbance of isotopic systematics by coupled dissolution-reprecipitation. Geochim Cosmochim Acta 269:398–412. https://doi.org/10.1016/j.gca.2019.10.024

Wen G, Bi SJ, Li JW (2016) Role of evaporitic sulfates in iron skarn mineralization: a fluid inclusion and sulfur isotope study from the Xishimen deposit, Handan-Xingtai district. North China Craton Miner Deposita 52(4):495–514. https://doi.org/10.1007/s00126-016-0674-8

Wen G, Li JW, Hofstra AH, Koenig AE, Lowers HA, Adams D (2017) Hydrothermal reequilibration of igneous magnetite in altered granitic plutons and its implications for magnetite classification schemes: insights from the Handan-Xingtai iron district, North China Craton. Geochim Cosmochim Acta 213:255–270. https://doi.org/10.1016/j.gca.2017.06.043

Whitney JA (1984) Fugacities of sulfurous gases in pyrrhotite-bearing silicic magmas. Am Mineral 69:69–78

Williams ML, Jercinovic MJ, Harlov DE, Budzyń B, Hetherington CJ (2011) Resetting monazite ages during fluid-related alteration. Chem Geol 283(3–4):218–225. https://doi.org/10.1016/j.chemgeo.2011.01.019

Williams ML, Jercinovic MJ, Hetherington CJ (2007) Microprobe monazite geochronology: understanding geologic processes by integrating composition and chronology. Annu Rev Earth Planet Sci 35:137–175. https://doi.org/10.1146/annurev.earth.35.031306.140228

Xie Q, Zhang Z, Hou T, Jin Z, Santosh M (2017) Geochemistry and oxygen isotope composition of magnetite from the Zhangmatun deposit, North China Craton: implications for the magmatic-hydrothermal evolution of Cornwall-type iron mineralization. Ore Geol Rev 88:57–70. https://doi.org/10.1016/j.oregeorev.2017.04.014

Xing L, Trail D, Watson EB (2013) Th and U partitioning between monazite and felsic melt. Chem Geol 358:46–53. https://doi.org/10.1016/j.chemgeo.2013.07.009

Xu DR, Kusiak MA, Wang ZL, Chen HY, Bakun-Czubarow N, Wu CJ, Konečný P, Hollings P (2015) Microstructural observation and chemical dating on monazite from the Shilu Group, Hainan Province of South China: implications for origin and evolution of the Shilu Fe–Co–Cu ore district. Lithos 216–217:158–177. https://doi.org/10.1016/j.lithos.2014.12.017

Xu W, Liu FL, Wang F, Santosh M, Dong YS (2019) Paleoproterozoic tectonic evolution of the Jiao-Liao-Ji Belt North China Craton: geochemical and isotopic evidence from ca. 2.17 Ga felsic tuff. Geol J. https://doi.org/10.1002/gj.3380

Yan XL, Chen B (2014) Chemical and boron isotopic compositions of tourmaline from the paleoproterozoic Houxianyu borate deposit, NE China: implications for the origin of borate deposit. J Asian Earth Sci 94:252–266. https://doi.org/10.1016/j.jseaes.2014.05.021

Yang H, Wang W, Liu JH (2017) Zircon U–Pb dating and its geological significance of granitic pegmatites from the Kuandian and Sanjiazi area in eastern Liaoning province. Acta Petrol Sin 33:2675–2688 **(In Chinese with English abs)**

Yavuz F, Yıldırım DK (2018) A Windows program for calculation and classification of epidote-supergroup minerals. Periodico Di Mineralogia 87:269–285. https://doi.org/10.2451/2018PM7808

Yin A, Nie S (1996) Phanerozoic palinspastic reconstruction of China and its neighboring regions. In: Yin A, Harrison TM (eds) The tectonic evolution of asia. Cambridge University Press, New York, pp 285–442

Yu B, Zeng Q, Frimmel HE, Wang Y, Guo W, Sun G, Zhou T, Li J (2018) Genesis of the Wulong gold deposit, northeastern North China Craton: constraints from fluid inclusions, H-O-S-Pb isotopes, and pyrite trace element concentrations. Ore Geol Rev 102:313–337. https://doi.org/10.1016/j.oregeorev.2018.09.016

Zhang P, Kou L, Zhao Y, Bi Z, Sha D, Han R, Li Z (2020) Genesis of the Wulong gold deposit, Liaoning Province, NE China: constrains from noble gases, radiogenic and stable isotope studies. Geosci Front 11(2):547–563. https://doi.org/10.1016/j.gsf.2019.05.012

Zhang QS (1988) Early Proterozoic tectonic styles and associated mineral deposits of the North China platform. Precambr Res 39(1–2):1–29. https://doi.org/10.1016/0301-9268(88)90047-2

Zhao GC, Cawood PA, Li SZ, Wilde SA, Sun M, Zhang J, He YH, Yin CQ (2012) Amalgamation of the North China Craton: key issues and discussion. Precambr Res 222–223:55–76. https://doi.org/10.1016/j.precamres.2012.09.016

Zhao GC, Sun M, Wilde SA, Li SZ (2005) Late Archean to paleoproterozoic evolution of the North China Craton: key issues revisited. Precambr Res 136(2):177–202. https://doi.org/10.1016/j.precamres.2004.10.002

Zhao GC, Wilde SA, Cawood PA, Lu LZ (1998) Thermal evolution of archean basement rocks from the eastern part of the North China Craton and its bearing on tectonic setting. Int Geol Rev 40:706–721. https://doi.org/10.1080/00206819809465233

Zhao HZ, Yang SS, Li H (2009) Geologic features of Baiyun gold ore deposit and discussion of the genesis. Non-Ferrous Mining Metal 25(3):4–7 **(in Chinese with English abstract)**

Zhong JR, Guo ZT (1988) The geological characteristics and metallogenetic control factors of the Liangshanguan uranium deposit, northeast China. Precambr Res 39:51–64. https://doi.org/10.1016/0301-9268(88)90050-2

Zhu XK, O'Nions RK (1999) Zonation of monazite in metamorphic rocks and its implications for high temperature thermochronology: a case study from the Lewisian terrain. Earth Planet Sci Lett 171(2):209–220. https://doi.org/10.1016/S0012-821X(99)00146-6

Zou Y, Zhai MG, Santosh M, Zhou LG, Zhao L, Lu JS, Shan HX (2017) High-pressure pelitic granulites from the Jiao-Liao-Ji Belt, North China Craton: a complete P–T path and its tectonic implications. J Asian Earth Sci 134:103–121. https://doi.org/10.1016/j.jseaes.2016.10.015

Zou Y, Zhai MG, Santosh M, Zhou LG, Zhao L, Lu JS, Liu B, Shan HX (2018) Contrasting P–T–t paths from a Paleoproterozoic metamorphic orogen: petrology, phase equilibria, zircon and monazite geochronology of metapelites from the Jiao-Liao-Ji belt, North China Craton. Precambr Res 311:74–97. https://doi.org/10.1016/j.precamres.2018.04.010

Zou Y, Zhai MG, Zhou LG, Zhao L, Lu JS, Wang YQ, Shan HX (2019) Relics of a paleoproterozoic orogen: New petrological, phase equilibria and geochronological studies on high-pressure pelitic granulites from the Pingdu-Laiyang areas, southwest of the Jiaobei terrane, North China Craton. Precambr Res 322:136–159. https://doi.org/10.1016/j.precamres.2018.12.01